© 2022. Published by The Company of Biologists Ltd | Development (2022) 149, dev200342. doi:10.1242/dev.200342

RESEARCH ARTICLE

Nrf2 dictates the neuronal survival and differentiation of embryonic zebrafish harboring compromised alanyl-tRNA synthetase

Binbin Jin[1,*], Liqin Xie[1,*], Dan Zhan[1], Luping Zhou[1], Zhi Feng[1], Jiangyong He[1], Jie Qin[1], Congjian Zhao[2], Lingfei Luo[1,‡] and Li Li[3,‡]

ABSTRACT

tRNA synthetase deficiency leads to unfolded protein responses in neuronal disorders; however, its function in embryonic neurogenesis remains unclear. This study identified an *aars1*$^{cq71/cq71}$ mutant zebrafish allele that showed increased neuronal apoptosis and compromised neurogenesis. *aars1* transcripts were highly expressed in primary neural progenitor cells, and their aberration resulted in protein overloading and activated Perk. *nfe2l2b*, a paralog of mammalian *Nfe2l2*, which encodes Nrf2, is a pivotal executor of Perk signaling that regulates neuronal phenotypes in *aars1*$^{cq71/cq71}$ mutants. Interference of *nfe2l2b* in *nfe2l2b*$^{\Delta 1/\Delta 1}$ mutants did not affect global larval development. However, *aars1*$^{cq71/cq71}$;*nfe2l2b*$^{\Delta 1/\Delta 1}$ mutant embryos exhibited increased neuronal cell survival and neurogenesis compared with their *aars1*$^{cq71/cq71}$ siblings. *nfe2l2b* was harnessed by Perk at two levels. Its transcript was regulated by Chop, an implementer of Perk. It was also phosphorylated by Perk. Both pathways synergistically assured the nuclear functions of *nfe2l2b* to control cell survival by targeting *p53*. Our study extends the understanding of tRNA synthetase in neurogenesis and implies that Nrf2 is a cue to mitigate neurodegenerative pathogenesis.

KEY WORDS: Aars1, Nrf2, UPR, Perk, Neuronal apoptosis, Zebrafish

INTRODUCTION

The sophisticated synthesis and precise modification of nascent proteins are tightly regulated by a set of intracellular structures, particularly the endoplasmic reticulum (ER) (Pobre et al., 2019). Errors in protein synthesis and protein folding usually lead to ER stress and unfolded protein response (UPR) (Walter and Ron, 2011). When the UPR is mild and can be handled properly, adaptive degradation of the misfolded protein is promoted by active spliced X-box-binding protein 1 (XBP1), which is mainly produced by the transautophosphorylated iron-responsive element 1α (IRE) (Grandjean et al., 2020). In parallel, the ATF6 axis is involved in the attenuation of the UPR to promote cell survival (Yu et al., 2017). When intensive and/or chronic stress is overloaded, cell apoptosis occurs via induction of PERK (EIF2AK3) through its oligomerization and the phosphorylation of multiple targets, in particular EIF2A, to inhibit a general panel of proteins (Wang and Kaufman, 2016). ATF4 selectively activates the cell apoptosis program through cooperation with its target, CHOP (DDIT3) (Hu et al., 2018). The three branches of the UPR pathway coordinately determine the cell conditions (Binet and Sapieha, 2015).

The transcription factor NRF2 is encoded by the nuclear factor erythroid-derived 2-like 2 gene (*NFE2L2*). It has been proposed to be a master regulator of external stresses to promote cell survival (Baumel-Alterzon et al., 2021). However, multiple functions of NRF2 have recently been reported. Phosphorylated NRF2 has been linked to PERK in the immunosuppression of tumors (Mohamed et al., 2020). The activation of *nfe2l2a*, a zebrafish paralog of *Nfe2l2*, attenuates ER stress in *pmm2*-deficient larval livers (Mukaigasa et al., 2018). Several studies have reported that activated NRF2 serves as a substrate for caspase-3 (-like) proteases and functions together with P38 or P53 (TP53) to induce apoptotic processes (Bonay et al., 2015; Ohtsubo et al., 1999). The various outcomes of NRF2 indicate its complicated and context-dependent effects (Menegon et al., 2016).

The *AARS1* gene encodes alanyl-tRNA synthetase (AlaRS), which is composed of three domains: an N-terminal aminoacylation domain, an editing domain and a C-terminal domain. It conducts a conserved aminoacylation reaction to charge alanine amino acids on the corresponding cognate tRNAs. This process is essential for the translation of the genetic code in protein or peptide synthesis. In the *Aars1*$^{sti/sti}$ mutant mice that harbored a C-to-A mutation at amino acid 734 in the editing domain of aminoacyl-tRNA synthetase (Aars1), notable loss of Purkinje cells and the development of neurodegenerative-like syndromes were observed (Lee et al., 2006). This phenotype was caused by the production of serine-mischarged-tRNA^{Ala}, which led to UPR in the cerebellar Purkinje cells. Ankrd16, a vertebrate-specific protein containing ankyrin repeats, partially alleviated the degeneration of cerebellar Purkinje cells in *Aars1*$^{sti/sti}$ mutant mice by binding to the catalytic domain of AlaRS to capture the misactivated serine and prevent mischarging (Vo et al., 2018). In humans, 11 missense mutations in three functional domains of *AARS1* have been identified in Charcot-Marie-Tooth type 2N, an autosomal-dominant inherited form of axonal neuropathy (McLaughlin et al., 2012; Motley et al., 2015; Simons et al., 2015). These phenomena indicate the indispensable role of *AARS1* in the control of proteostasis and UPR intensity in neuronal development and neurodegenerative diseases.

Neurogenesis in zebrafish is initiated by the specification of neural progenitor cells (NPCs) after the establishment of the neuroectoderm (Schmidt et al., 2013). Deficiency in the production and maintenance of NPCs leads to compromised neurogenesis (Li et al., 2020). In the present study, we performed a large-scale

[1]Institute of Developmental Biology and Regenerative Medicine, Key Laboratory of Freshwater Fish Reproduction and Development, Ministry of Education, Southwest University, Chongqing 400715, China. [2]Chongqing Engineering Research Center of Medical Electronics and Information Technology, School of Biomedical Engineering and informatics, Chongqing University of Posts and Telecommunications, Chongqing 40065, China. [3]Research Center of Stem Cells and Ageing, Chongqing Institute of Green and Intelligent Technology, Chinese Academy of Sciences, Chongqing 400714, China.
*These authors contributed equally to this work

‡Authors for correspondence (lili@cigit.ac.cn; lluo@swu.edu.cn)

L.Z., 0000-0002-9539-0085; J.Q., 0000-0002-4986-8113; C.Z., 0000-0002-2920-6286; L. Luo, 0000-0002-5318-8137; L. Li, 0000-0002-6920-3311

Handling Editor: François Guillemot
Received 8 November 2021; Accepted 28 July 2022

Development (2022) 149, dev200342. doi:10.1242/dev.200342

mutant screening and identified an *aars1*$^{cq71/cq71}$ mutant zebrafish allele that manifested compromised neurogenesis caused by intensive cell apoptosis of NPCs. Together with the threonyl-tRNA synthetase mutant, *tars1*$^{cq16/cq16}$ (Cao et al., 2016), we revealed that compromised aminoacyl-tRNA synthetase in the NPCs led to UPR reactions and resultant cell apoptosis by the activation of Perk signaling. *nfe2l2b*, but not *nfe2l2a*, acted as a downstream executor by targeting *p53*. Our study reveals Nrf2 as a regulative molecule of *p53* in Perk-mediated cell apoptosis and provides clues on the progress and treatment of neurodegenerative disorders.

RESULTS

Identification of an ethylnitrosourea (ENU) mutant with compromised neurogenesis

To explore the molecules involved in neurogenesis, we performed an unbiased large-scale screening of a candidate pool of ethylnitrosourea (ENU)-induced mutagenesis (Cao et al., 2016). We examined the signals of *neurogenic differentiation 1* (*neurod1*), which is mainly expressed in postmitotic neuronal cells, by whole-mount *in situ* RNA hybridization (WISH). The recessive *ENU* mutant allele that presented an obvious reduction in *neurod1*$^{+}$ signals was fortuitously recovered (Fig. 1A). We named it as 'Chongqing number 71' (cq71) mutant (referred to as Mut$^{cq71/cq71}$ herein). Several genes that encode components of neuronal and glial cells were further analyzed in Mut$^{cq71/cq71}$ by characterizing either corresponsive reporter lines or transcript levels. The signals of neural-specific beta-tubulin (NBT) in pan-neuronal cells, *sox2* and *neurog1* in NPCs, Elav-like neuron-specific RNA-binding protein 3 (HuC) and NGF/*microtube-associated protein2* (*map2*) in young neurons, alpha-tubulin ortholog (*tuba1b*) in mature neurons, *olig2* in eurydendroid neurons in the cerebellum, and *glial fibrillary acidic protein* (*gfap*) in astrocytes and radial glial cells showed marked reduction in the brains, but not spinal cords, of Mut$^{cq71/cq71}$ compared with their wild-type (WT) and heterozygous siblings at 2.5-3 dpf (Fig. 1A, Fig. S1A,B). The size of 3 dpf midbrain was 75,973±2162 µm^2 in Mut$^{cq71/cq71}$ larvae compared with 91,176±2063 µm^2 in WT counterparts (Fig. S1C). Mut$^{cq71/cq71}$ larvae did not survive beyond 7 dpf (Fig. S1D). The behavior

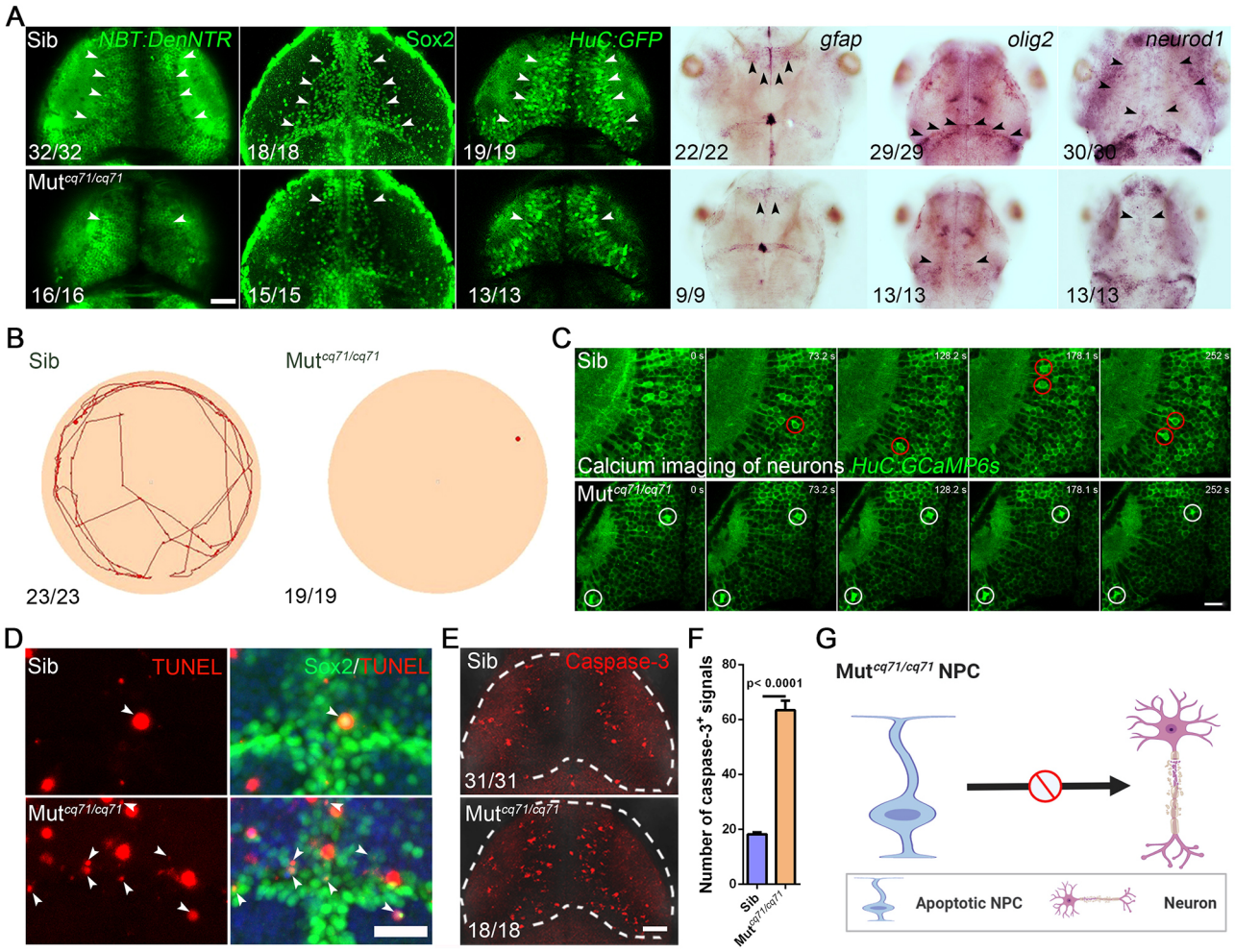

Fig. 1. Phenotype characterization of Mut$^{cq71/cq71}$ embryos. (A) Whole-mount *in situ* RNA hybridization (WISH) and fluorescent images of 3 dpf larval brain. The white and black arrowheads indicate the fluorescence and WISH signals, respectively. (B) Representative movement traces of 3 dpf larvae. (C) Timelapse frames of Ca^{2+} sparks in the midbrains of *Tg(HuC:GCaMP6s)*. The red and white circles indicate the active (red) and dead (white) neurons with Ca^{2+} transients or intensive Ca^{2+} signals, respectively. (D) Immunofluorescent images of TUNEL and Sox2 in the transverse sections of 3 dpf midbrains. The white arrowheads indicate the colocalization of TUNEL^{+} and Sox2^{+} signals. (E,F) Representative immunofluorescent images (E) and quantification (F) of Caspase-3^{+} signals in 3 dpf midbrains (highlighted by white dashed lines) (mean±s.e.m.; sibling, 18.24±0.71 *n*=17; Mut$^{cq71/cq71}$, 63.41±3.51 *n*=21; two independent clutches; unpaired two-tailed Student's *t*-test). (G) Schematic illustration of increased neural progenitor cell (NPC) apoptosis and compromised neurogenesis in Mut$^{cq71/cq71}$ brains. Scale bars: 20 µm.

Development (2022) 149, dev200342. doi:10.1242/dev.200342

recordings indicated that 3 dpf WT larvae spontaneously moved at 0.19±0.05 cm/s to cover a distance of 81.74±20.34 cm during a 5 min recording. However, Mut$^{cq71/cq71}$ larvae exhibited compromised spontaneous mobility (Fig. 1B, Fig. S1E,F, Movie 1). The WT larvae rapidly responded to the external stimuli of either needle-touch or light reduction and altered the speed to 0.22±0.02 cm/s or 0.15±0.02 cm/s, respectively. However, the Mut$^{cq71/cq71}$ larvae remained mostly frozen (Fig. S1G-L, Movies 2 and 3). Although Mut$^{cq71/cq71}$ larvae occasionally acted upon the stimuli, their movement speeds were markedly reduced compared with those of their WT siblings (Fig. S1I,L). Accordingly, neuronal activities indicated by Ca^{2+} transients of various types were frequently detected in WT transgenic *Tg(HuC:GCaMP6s)* midbrains; however, they were barely seen in the Mut$^{cq71/cq71}$ *Tg(HuC:GCaMP6s)* (Fig. 1C, Movie 4). These phenotypes indicated compromised neurogenesis in Mut$^{cq71/cq71}$ embryos, suggesting increased cell death and/or reduced proliferation of NPCs in this scenario. The staining results indicated that phospho-Histone 3 (PH3$^+$) signals surprisingly displayed an increment in Mut$^{cq71/cq71}$ brains at 2.5 dpf (Fig. S1M,N). However, the terminal deoxynucleotidyl transferase dUTP nick end labeling (TUNEL)$^+$ signals that were rarely detected in Sox2$^+$ NPCs in WT larvae were easily visible in Mut$^{cq71/cq71}$ counterparts (Fig. 1D). Simultaneously, Acridine Orange (AO) and Caspase-3 signals increased notably in the Mut$^{cq71/cq71}$ brains, but not in the spinal cord, when compared with those in their WT and heterozygous siblings (Fig. 1E,F, Fig. S1O-S). The expanded AO$^+$ signals were collected but not effectively cleared by Coro1a-Dsred$^+$ microglia (Li et al., 2012) and exhibited enlarged foci in the Mut$^{cq71/cq71}$ brains (Fig. S1S). These results indicated increased apoptosis of NPCs and compromised neurogenesis in the Mut$^{cq71/cq71}$ brains (Fig. 1G).

aars1 intrinsically regulates neuronal survival and neurogenesis

To unveil the gene responsible for Mut$^{cq71/cq71}$ mutants, we utilized a total of 1890 meioses to perform genetic linkage analysis and restricted the location to chromosome 18, with ∼1.35 and 0.92 centimorgan intervals to ZK225B14 and ZK261F4, respectively (Fig. 2A). One recombination was discovered by sequencing the selected single-nucleotide polymorphism (SNP) 1 and 2 in this region, further narrowing the mutation to a 0.13 Mb spacing (Fig. 2A). Four genes were annotated in this fragment according to the information from Ensembl (http://asia.ensembl.org/index.html). A point mutation (T-to-A) in exon 5 of *aars1* was identified in the Mut$^{cq71/cq71}$ embryos (Fig. 2B, Fig. S2A). There are four isoforms of *aars1* in zebrafish. However, only 201 (ENSDART00000076695.6), a short isoform, and 202 (ENSDART00000100401.6), encoding the whole functional domain of *aars1*, were successfully amplified from the cDNA library of 3 dpf embryos. The T-to-A mutation in *aars1*$^{cq71/cq71}$ caused an alteration from UGU to UGA at position 171, producing a truncated protein with a premature stop codon (Fig. 2B, Fig. S2B). Western blot analysis indicated that the mutant forms of HA-*aars1* were unstable, and the protein levels of Aars1 were markedly reduced by 87%, in the *aars1*$^{cq71/cq71}$ brains compared with the brains of their WT siblings (P=0.0002) (Fig. 2C, Fig. S2C). Furthermore, WISH showed a dramatic reduction in *aars1* transcripts in the *aars1*$^{cq71/cq71}$ mutants compared with the WT siblings (Fig. S2N). The transcription levels of the nonsense-mediated mRNA decay (NMD)-related genes, including *upf1* and *upf3b*, but not *upf3a*, were significantly increased in *aars1*$^{cq71/cq71}$ mutants (Fig. S2D), implying an NMD (Cheruiyot et al., 2021) promoting rapid degradation of *aars1* mRNA in *aars1*$^{cq71/cq71}$ mutants. These data indicated that the *aars1*$^{cq71/cq71}$ mutant was a null allele.

The zebrafish full-length Aars1 (Aars1^{202}) protein shared 81.88% and 82.61% similarity with its human and mouse counterparts, respectively (Fig. S2E). Supplementation of *aars1*^{202} (referred to as *aars1* in subsequent sections) and even human *AARS1* in the *aars1*$^{cq71/cq71}$ mutant embryos rescued the phenotypes of Sox2$^+$ NPCs and reduced the TUNEL$^+$ and AO$^+$ signals (Fig. 2D, Fig. S2F,G). An additional *aars1*$^{\Delta10/\Delta10}$ mutant allele with a 10 bp deletion was generated. The *aars1*$^{\Delta10/\Delta10}$ mutation caused premature termination of the Aars1 protein in the amino acid activation domain (Fig. 2B, Fig. S2A), which led to a dramatic reduction in its protein levels to 15% of that in siblings (Fig. 2C, Fig. S2C). Similar to the *aars1*$^{cq71/cq71}$ mutant embryos, the *aars1*$^{\Delta10/\Delta10}$ mutants manifested intensive atrophy of the midbrain, an increase in AO$^+$ signals, and a reduction in Sox2$^+$, HuC$^+$ and *neurod1*$^+$ pools compared with their WT siblings (Fig. 2E,F, Fig. S2H). The result of a complementary assay by mating *aars1*$^{cq71/cq71}$ with *aars1*$^{\Delta10/\Delta10}$ allele indicated the same declined *aars1* transcripts and neural-defective signatures as those seen in either *aars1*$^{cq71/cq71}$ or *aars1*$^{\Delta10/\Delta10}$ mutant alleles (Fig. S2I-K). Interference of *aars1* using ribonucleoproteins (RNPs) (Cas9 protein/synthetic crRNA:tracrRNA duplex technology) (Kroll et al., 2021) was further investigated. Among the six predicted target sites by Integrated DNA Technologies (IDT), three targets of crRNAs at loci A, B and D showed the highest mutated efficiency of 94%, 90% and 65%, respectively, according to the ratio of head loop-PCR/standard-PCR (Kroll et al., 2021) (Fig. S2L). The levels of Aars1 protein were reduced by 77% in the *aars1* F0 group after the combinational application of these crRNAs compared with those in the controls (P=0.0016) (Fig. S2M). Annexin V staining was applied as an indicator, because it has a high affinity for phosphatidylserine of dying cells (Balaji et al., 2013). A marked increase in Annexin V$^+$ signals was detected in *aars1* F0 embryos treated with *aars1* RNPs compared with controls (Fig. 2G), corroborating the increased neuronal apoptosis and compromised neurogenesis upon Aars1 deficiency.

The *aars1* transcript appeared even at the one-cell stage of the fertilized embryos and was almost evenly present in the cells at the 50% epiboly stage (Fig. S2N). Following this, the transcript was highly expressed in the midbrain and digestive organs (Fig. S2O). In the midbrain, double staining and quantitative PCR (qPCR) results indicated that the *aars1* transcript was highly detected in the *sox2*$^+$, *NBT*$^+$ and *HuC*$^+$ cells, detected to a lower extent in the *neurod1*$^+$ and *olig2*$^+$ cells, and was limited in the *coro1a*$^+$ microglial cells (Fig. 2H, Fig. S2P), implying its enrichment in NPCs and intrinsically regulated neurogenesis. Therefore, we provided *aars1* in the pan-neuronal cells by fusing its cDNA sequence to the *NBT* promoter (Thomas-Jinu et al., 2017). This assay could supply *aars1* in Sox2$^+$ NPCs, based on the clear detection of Sox2$^+$ signals in the NBT-DenNTR$^+$ cells (Fig. S2Q). Continual supplementation of *NBT-aars1* in *Tg(NBT:aars1)* slightly lowered the AO$^+$ signals but markedly mitigated the intensity of AO$^+$ phenotypes in *aars1*$^{cq71/cq71}$ mutants to a level comparable with that in WT siblings (Fig. 2I,J). Furthermore, a transplantation assay was performed following previous instruction (Zou and Wei, 2010). An equal number of cells (30-50) was isolated from the blastomeres of WT or *aars1* F0 animals harboring NBT-DenNTR background. These cells were transplanted into the recipients (Fig. 2K). Examination of Annexin V indicated that the signals did not present notable alterations in the *aars1*$^{cq71/cq71}$ mutant recipients

Development (2022) 149, dev200342. doi:10.1242/dev.200342

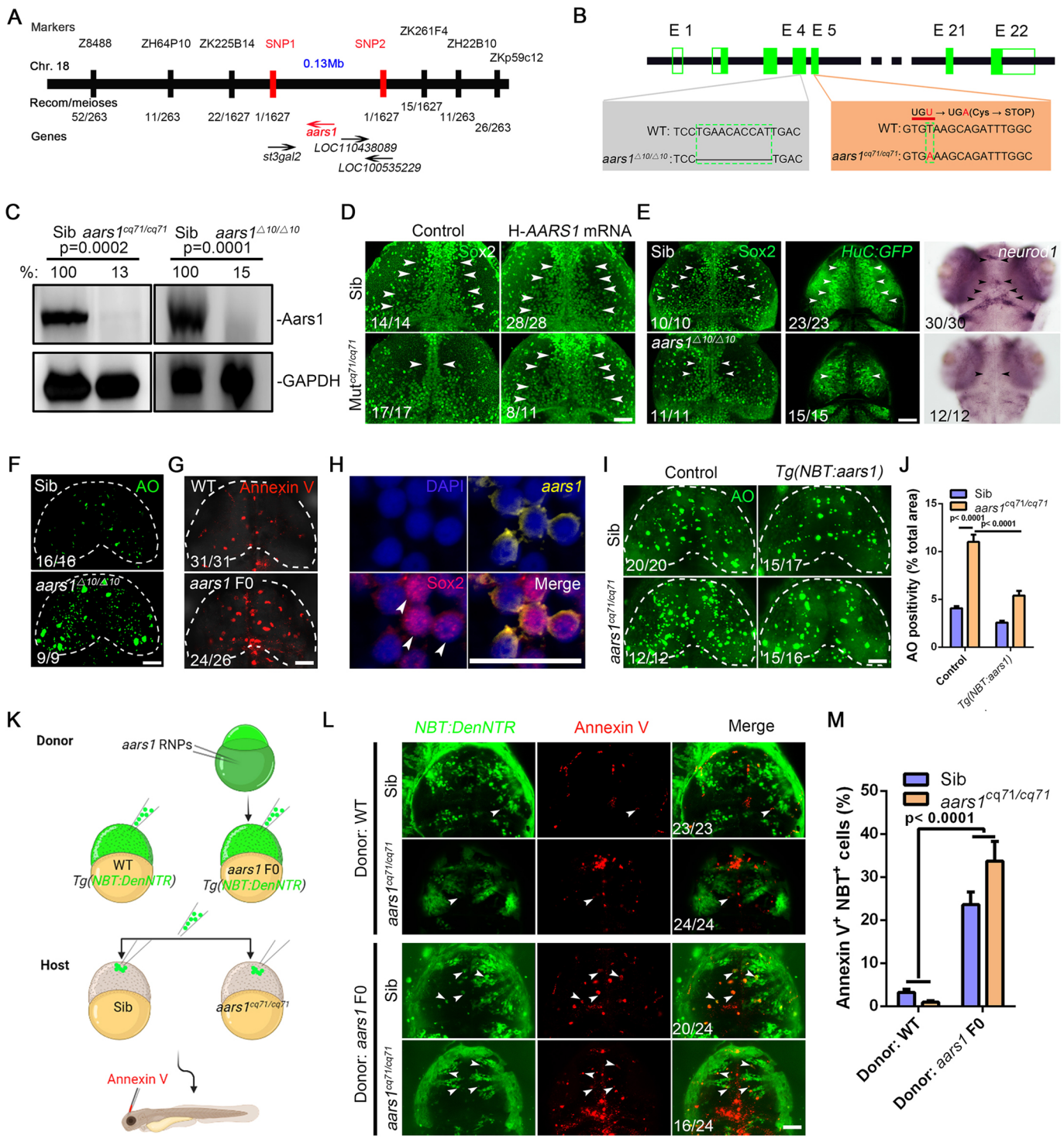

Fig. 2. *aars1* intrinsically regulates neural survival and neurogenesis. (A) Schedules of the bulk segregation and fine-mapping strategies in identifying mutant genes. (B) Diagram of two types of *aars1* mutant alleles. The gray box shows 10 bp deletion at exon 4 of *aars1*$^{\Delta10/\Delta10}$; the orange box indicates an alteration of T to A at exon 5 of *aars1*$^{cq71/cq71}$. All these mutants led to the early termination of Aars1 protein. (C) Western blot of Aars1. The protein levels of Aars1 reduced by 87% (*P*=0.0002) and 85% (*P*=0.0001) in the *aars1*$^{cq71/cq71}$ and *aars1*$^{\Delta10/\Delta10}$ mutants, respectively, compared with those in their siblings. (D) Immunofluorescent images of Sox2 in the midbrains of siblings and *aars1*$^{cq71/cq71}$ after injecting H-*AARS1* mRNA. The white arrowheads indicate the Sox2^{+} signals. (E) Immunofluorescent (left and middle column) and WISH (right column) images of Sox2 (white arrowheads, left column), GFP (white arrowheads, middle column) and *neurod1* (black arrowheads). (F,G) Fluorescent images of Acridine Orange (AO)$^{+}$ (F) and Annexin V^{+} (G) signals in the midbrains. (H) Immunofluorescent images of double staining of *aars1* transcript with Sox2. (I,J) Representative fluorescent images (I) and quantification (J) of AO^{+} signals in the midbrains [mean±s.e.m.; control: sibling, 4.07±0.22 *n*=7; *aars1*$^{cq71/cq71}$, 11.01±0.76 *n*=6; *Tg(NBT:aars1)*: sibling, 2.57±0.18 *n*=17; *aars1*$^{cq71/cq71}$, 5.39±0.49 *n*=15; two independent clutches; two-way ANOVA]. (K) Schema for the transplantation experiment. (L) Confocal imaging of NBT-DenNTR^{+} and Annexin V^{+} signals at 3 dpf. The arrowheads indicate the NBT-DenNTR^{+} and Annexin V^{+} signals. (M) The percentage of Annexin V^{+} signals in the NBT-DenNTR^{+} cells in L (mean±s.e.m.; WT donor: sibling, 3.22±0.70 *n*=30; *aars1*$^{cq71/cq71}$, 0.93±0.38 *n*=23; *aars1* F0 donor: sibling, 23.59±2.98 *n*=19; *aars1*$^{cq71/cq71}$, 33.72±4.59 *n*=18; two independent clutches; two-way ANOVA). Scale bars: 20 µm.

Development (2022) 149, dev200342. doi:10.1242/dev.200342

after accepting the NBT^{+} blastomere cells from the WT siblings, but were elevated dramatically after receiving the donors of the *aars1* F0 origin compared with their control groups (Fig. 2L,M). Taken together, these results indicate that *aars1* is cell-autonomously required and functionally conserved for neuronal survival and development.

ER stress and UPR are elevated to induce NPC apoptosis in *aars1*$^{cq71/cq71}$ mutants

The molecular mechanisms underpinning *aars1* in neurogenesis require further investigation. To this end, single-cell RNA sequencing (scRNA-seq) was performed (Fig. S3A). In total, 17,519 and 14,465 cells were obtained from 2 dpf siblings and *aars1*$^{cq71/cq71}$ mutant midbrains, respectively. Comparable sequencing depths (18,129 and 22,921 reads/cell), median unique molecular identifier (UMI) counts (1964 and 2844 UMI/cell), and median gene numbers (949 and 1211 genes/cell) were obtained from WT siblings and *aars1*$^{cq71/cq71}$ mutants. We classified the cell types of all samples and mapped the resulting reads to the zebrafish genome for unbiased clustering using Seurat software. Twelve major cell clusters were identified (Fig. S3B). Among them, nine neuronal clusters [GABAergic neurons, glutamatergic neurons, thalamic neurons, progenitor neurons (differentiating), progenitors, radial glial cells (RGCs), optic tectum neurons, vagal neurons and oligodendrocyte progenitor cells (OPCs)], based on the top ten genes in each cluster, were predominant (Fig. 3A-C). Intriguingly, cluster 4 progenitor cells were notably enlarged to 65% in the *aars1*$^{cq71/cq71}$ mutants, in contrast to the detectable shrinkage of other clusters (Fig. 3D). Evaluation of 20 aminoacyl-tRNA synthetases (ARSs) revealed that *aars1* transcripts were singularly enriched in cluster 4 (Fig. 3E, Fig. S3C). Cluster 4 was further divided into three subtypes, and *aars1* was more precisely positioned in subpopulations 1 and 2, the oldest stages of the progenitors that occupied more than half of this pool (Fig. 3E-G).

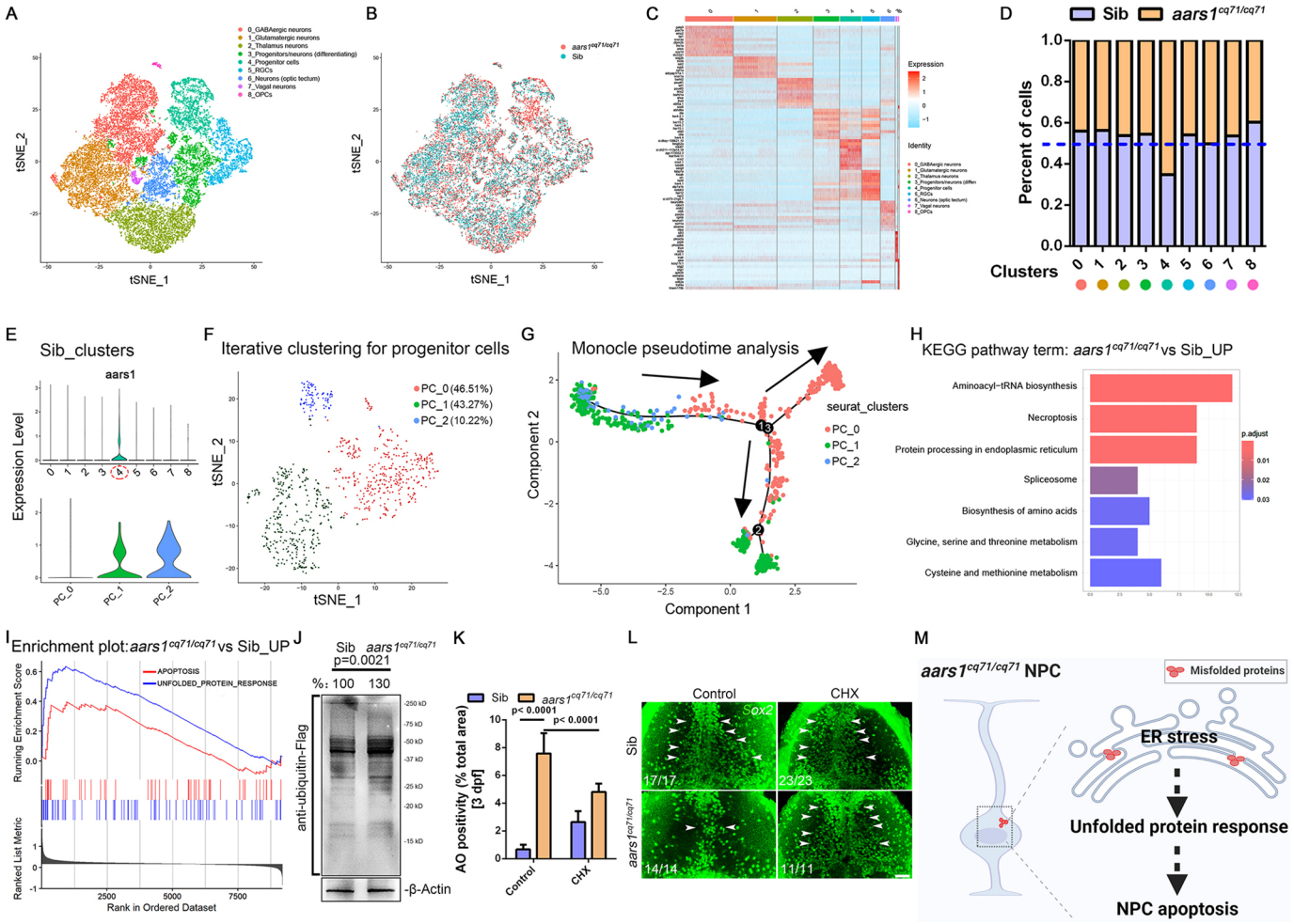

Fig. 3. Profiles of neural cell clusters in WT and *aars1*$^{cq71/cq71}$ mutants. (A) Graph-based clustering of neural cells. RGCs, radial glial cells; OPCs, oligodendrocyte progenitor cells. (B) t-SNE plot of the integration of neural cell clusters. (C) Heat map of the top ten transcript levels. (D) The cell proportions of distinct clusters in siblings and *aars1*$^{cq71/cq71}$ mutants. (E) Violin plot of *aars1* expression in neural cell (top) and progenitor cell (PC) (bottom) clusters in F. (F) t-SNE plot of PC clusters in siblings. (G) PC cluster trajectories of pseudotime by Monocle; colors depict the cell clusters in F. The arrows and numbers represent pseudotime and the decision point of progenitor cells, respectively. (H) Kyoto Encyclopedia of Genes and Genomes (KEGG) pathway term of upregulated genes in *aars1*$^{cq71/cq71}$ PCs. (I) Gene set enrichment analysis (GSEA) enrichment plot of upregulated pathways (apoptosis, unfolded protein response) in *aars1*$^{cq71/cq71}$ mutants. (J) Western blot results of protein ubiquitylation in brain lysates after injecting FLAG-tagged ubiquitin plasmid. The ubiquitylation levels increased by 30% in the *aars1*$^{cq71/cq71}$ mutants compared with those in siblings (P=0.0021). (K) Quantification of AO^{+} signals [mean±s.e.m.; control: sibling, 0.67±0.13 n=7; *aars1*$^{cq71/cq71}$, 7.58±0.60 n=6; cycloheximide (CHX): sibling, 2.64±0.26 n=8; *aars1*$^{cq71/cq71}$, 4.81±0.21 n=8; two independent clutches; two-way ANOVA]. (L) Immunofluorescent images of Sox2^{+} cells. White arrowheads indicate the Sox2^{+} signals. (M) Schematic illustration of unfolded protein response leading to NPC apoptosis in *aars1*$^{cq71/cq71}$ mutants. Scale bar: 20 µm.

Development (2022) 149, dev200342. doi:10.1242/dev.200342

These data were consistent with the intrinsic roles of *aars1* in the survival of NPCs and suggested the stalling of progenitor differentiation before apoptosis in the *aars1*$^{cq71/cq71}$ mutants. Information regarding the Kyoto Encyclopedia of Genes and Genomes (KEGG) pathway from cluster 4 revealed pronounced elevations in aminoacyl-tRNA biosynthesis signaling, necroptosis and protein processing in the ER (Fig. 3H). Gene Ontology (GO) analysis indicated a marked alteration of factors in the UPR and apoptotic pathways (Fig. 3I, Fig. S3D), pointing to protein overload and ER stress in the NPCs of the *aars1*$^{cq71/cq71}$ mutants. To this end, we injected FLAG-tagged ubiquitin constructs into WT siblings and *aars1*$^{cq71/cq71}$ mutant embryos, which were then detected using anti-FLAG antibodies. The levels of ubiquitin-modified protein fragments were increased by 30% in the administered *aars1*$^{cq71/cq71}$ mutant embryos compared with those in the WT siblings (P=0.0021) (Fig. 3J). However, when the protein loads were attenuated by cycloheximide (actidione, naramycin A; CHX), an antifungal antibiotic that inhibits protein and RNA synthesis (Klinge et al., 2011), the AO$^+$ and Sox2$^+$ cells in the *aars1*$^{cq71/cq71}$ mutants recovered to the levels in the WT siblings (Fig. 3K,L). These results indicated that the intensive UPR by misfolded proteins induced NPC apoptosis in *aars1*$^{cq71/cq71}$ mutants (Fig. 3M).

Perk signaling is responsible for NPC apoptosis in *aars1*$^{cq71/cq71}$ mutants

Protein overload causes ER stress. A prolonged UPR eventually leads to apoptosis (Guha et al., 2017). Indeed, the protein levels of BiP (Hspa5), a protein-folding chaperone (Wang et al., 2017), increased by 117% in the *aars1*$^{cq71/cq71}$ mutant brains compared with those in the brains of their WT siblings (P=0.0004) (Fig. 4A, Fig. S4A). The ER structures were severely distended and dilated in *aars1*$^{cq71/cq71}$ mutant brains compared with those in WT sibling brains (Fig. 4B, Fig. S4B). To determine the role of aggravated ER stress in excessive apoptosis of *aars1*$^{cq71/cq71}$ mutant NPCs, two chemicals, thapsigargin (Tg), a potent ER Ca^{2+} pump inhibitor (Sehgal et al., 2017), and tunicamycin (Tn), a protein glycosylation inhibitor (Guha et al., 2017), were used to treat WT embryos. The

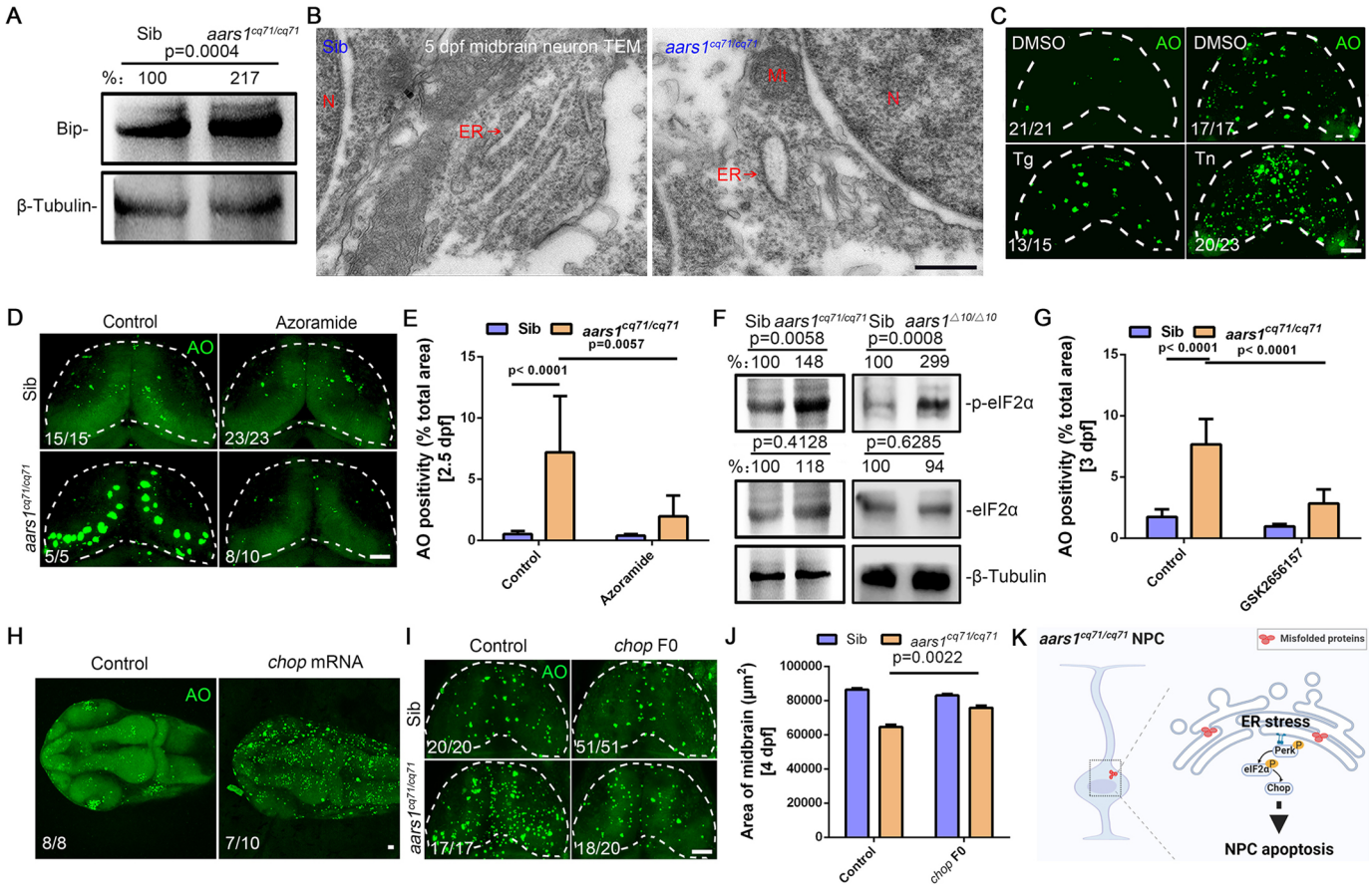

Fig. 4. Perk signaling controls neuronal apoptosis in *aars1*$^{cq71/cq71}$ mutants. (A) Western blot of Bip. Bip protein levels increased by 117% in the *aars1*$^{cq71/cq71}$ mutants compared with those in siblings (P=0.0004). (B) Endoplasmic reticulum structure by transmission electron microscopy. N, nucleus; ER, endoplasmic reticulum (red arrows); Mt, mitochondria. (C) Fluorescent images of AO$^+$ signals in the midbrains of WT embryos treated with thapsigargin (Tg) from 36 to 53 hpf (left column) or tunicamycin (Tn) from 2.5 to 3 dpf (right column). DMSO, dimethyl sulfoxide. (D,E) Representative fluorescent images (D) and quantification (E) of AO$^+$ signals in the midbrains (mean±s.e.m.; control: sibling, 0.53±0.06 n=16; *aars1*$^{cq71/cq71}$, 7.20±1.32 n=12; azoramide: sibling, 0.39±0.03 n=18; *aars1*$^{cq71/cq71}$, 1.97±0.46 n=14; two independent clutches; two-way ANOVA). (F) Western blot of p-eIF2α and eIF2α. The levels of p-eIF2α increased by 48% (P=0.0058) and 199% (P=0.0008) in the *aars1*$^{cq71/cq71}$ (left) and *aars1*$^{Δ10/Δ10}$ (right) mutants, respectively, compared with those in their siblings. (G) Quantification of AO$^+$ signals after treatment with GSK2656157 (mean±s.e.m.; control: sibling, 1.73±0.18 n=12; *aars1*$^{cq71/cq71}$, 7.66±0.65 n=10; GSK2657157: sibling, 0.97±0.05 n=12; *aars1*$^{cq71/cq71}$, 2.83±0.44 n=7; two independent clutches; two-way ANOVA). (H,I) Fluorescent images of AO$^+$ signals after injecting *chop* mRNA (H) or ribonucleoprotein (I). (J) Quantification of midbrain size (mean±s.e.m.; control: sibling, 86,414.22±876.09 n=14; *aars1*$^{cq71/cq71}$, 64,523.13±1402.89 n=9; *chop* F0: sibling, 83,041.39±889.31 n=12; *aars1*$^{cq71/cq71}$, 75,772.63±1359.52 n=21; two independent clutches; two-way ANOVA). (K) Schematic illustration of endoplasmic reticulum stress inducing NPC apoptosis through the Perk–Chop axis in *aars1*$^{cq71/cq71}$ mutants. Scale bars: 0.5 µm (B); 20 µm (C,D,H,I).

Development (2022) 149, dev200342. doi:10.1242/dev.200342

application of either molecule promoted the appearance of substantial AO^+ signals in the brains of cultured embryos (Fig. 4C). Conversely, significant mitigation of AO^+ phenotypes was observed when *aars1*$^{cq71/cq71}$ mutant embryos were incubated with azoramide, an ER stress inhibitor (Fu et al., 2015) (Fig. 4D,E).

In mammalian cells, ER stressors activate proximal UPR pathways through three major trans-ER membrane proteins, IRE1, ATF6 and PERK (Metcalf et al., 2020). We investigated the kinetics of these pathways by measuring the protein volume of phosphorylated (p)-eIF2α (as a direct readout of Perk activation) (Humeau et al., 2020), and the transcript amounts of *atf6* and 'unconventional' splicing of *xbp1* (reflecting Ire1 activation) (Guo et al., 2014) in the pooled WT sibling or *aars1*$^{cq71/cq71}$ mutant embryos. The protein levels of eIF2α, especially its activated form, p-eIF2α, were markedly elevated by 48% in the *aars1*$^{cq71/cq71}$ mutant brains compared with those in the brains of their WT siblings (P=0.0058) (Fig. 4F), indicating the activation of Perk signaling upon aberrant *aars1* function. Although the transcript levels of *atf6* and *ire1α* were notably increased in *aars1*$^{cq71/cq71}$ mutants (Fig. S4C), neither pathway was effectively functional, based on the results of the defective *xbp1* RNA splicing and the inability of the ATF6 inhibitor Ceapin A7 (Gallagher et al., 2016) to attenuate cell apoptosis in the *aars1*$^{cq71/cq71}$ mutants (Fig. S4D,E). To further assess the effects of Perk signaling, we interfered with Perk function by using GSK2656157, a specific Perk signaling inhibitor (Atkins et al., 2013), which decreased the p-eIF2α protein levels by 64% compared with the controls (P=0.0030) (Fig. S4F). Application of this chemical remarkably reduced the AO^+ signals in the *aars1*$^{cq71/cq71}$ mutant midbrains, which were not present in the samples that were treated with controls (Fig. 4G). Collectively, Perk activation during ER stress plays a crucial role in NPC apoptosis in *aars1*-deficient embryos. Atf4 and the pro-apoptotic transcription factor *chop* are responsible for Perk and eIF2α activity (Walter and Ron, 2011). Their expression levels increased markedly in *aars1*$^{cq71/cq71}$ mutant brains compared with those in the brains of their sibling counterparts (Fig. S4A,G). Additionally, overexpressing *chop* mRNA in WT embryos markedly induced the appearance of AO^+ signals (Fig. 4H). Conversely, injection of the designed *chop* RNPs, which efficiently mutated the F0 embryos by more than 70% in each target locus, significantly reduced the AO^+ signals in *aars1*$^{cq71/cq71}$ mutants compared with those in WT embryos (Fig. 4I, Fig. S4H,I). An enlarged pool of NBT-$DenNTR^+$ cells and increased sizes of the midbrain in the RNP-treated embryos were observed simultaneously (Fig. 4J, Fig. S4J). Autophagy has been reported to be regulated by Perk in zebrafish (Jia et al., 2015), and it is involved in tRNA synthetase-deficient cardioproteinopathy (Liu et al., 2014). However, examination of the protein levels of microtubule-associated protein light chain 3 (Lc3; Map1lc3b) and p62 by western blotting, together with the imaging of mCherry-Lc3-labeled autophagosomes and p62-characterized autophagy substrates in the neurons, indicated that their signals were limitedly altered in the *aars1*$^{cq71/cq71}$ mutants compared with those in the WT siblings (Fig. S4K-M). Collectively, these results indicated that activated Perk signaling in the *aars1*$^{cq71/cq71}$ mutants triggered NPC apoptosis via *chop* (Fig. 4K) but limitedly affected autophagy.

nfe2l2b as a key executor of the Perk pathway in the regulation of neuronal fate

The mechanism by which the PERK–CHOP axis regulates cell survival remains unclear. To address this, we established an *in vitro* cell culture assay to explore the key factors involved. The addition of Tn and Tg to HEK293T cells successfully induced an increase in annexin V^+ signals (Fig. 5A,B). In the groups treated with Tg and Tn, the levels of p-PERK elevated to 398% (P<0.0001) and 353% (P<0.0001), respectively, compared with the controls (Fig. 5A-C). We then focused on NRF2, a classical antioxidant transcription factor that plays a vital role in a wide spectrum of stress responses (Ma, 2013). Western blotting results indicated that the protein levels of NRF2 significantly elevated by 210% (P<0.0001) and 67% (P=0.0018) in the Tg and Tn groups, respectively, compared with the controls (Fig. 5D). Immunostaining data revealed a similarly notable increase, especially its phosphorylated form in the nucleus, upon application of these chemicals (Fig. 5D,E). Concordantly, treating HEK293T cell lines and WT zebrafish embryos with oltipraz, an Nrf2-specific activator (Magesh et al., 2012), exacerbated Annexin V^+ and AO^+ signals but reduced p-eIF2α protein levels by 32% relative to those in the control (P=0.0017) (Fig. 5F,G, Fig. S5A). There are two *Nfe2l2* paralogs in zebrafish, *nfe2l2a* and *nfe2l2b* (Fig. S5B). Pattern characterization using WISH indicated that both factors were maternally expressed (Fig. S5C). They were similarly detected in the brain and eyes and colocalized with NBT-$DenNTR^+$ cells (Fig. 5H, Fig. S5C). Interestingly, qPCR and fluorescence *in situ* hybridization (FISH) results indicated that the transcript levels of *nfe2l2b* were increased by 2.7-fold in *aars1*$^{cq71/cq71}$ NBT^+ cells (Fig. 5H,I, Fig. S5D), in contrast to the reduced levels of *nfe2l2a* at the same time (Fig. S5D). Activation of *nfe2l2a* has been reported to attenuate ER stress in *pmm2*-deficient larval livers (Mukaigasa et al., 2018); however, the functions of *nfe2l2b*, a paralog of *Nfe2l2*, have rarely been investigated. Delivery of exogenous *chop* mRNA and oltipraz significantly elevated the transcript levels of *nfe2l2b*, but showed reduced influence on *nfe2l2a* transcript levels (Fig. 5J, Fig. S5E). The application of *chop* RNPs led to opposite outcomes (Fig. 5K). Supplying *nfe2l2a* to the *aars1*$^{cq71/cq71}$ mutants showed limited effects on the mitigation of AO^+ and $Sox2^+$ signals (Fig. S5F,G). These data suggest that *nfe2l2b* functions downstream of the Perk–Chop axis in the regulation of neuronal apoptosis. Therefore, we injected one-cell embryos with *nfe2l2b* mRNA and performed AO staining. Surprisingly, overexpression of full-length *nfe2l2b* mRNA significantly increased AO^+ signals in WT midbrains but reduced the p-eIF2α protein levels by 26% (P=0.2332) (Fig. 5L, Fig. S5H). Conversely, we generated a *nfe2l2b* mutant allele with a 1 bp deletion, which led to a predictive premature stop codon in translation (Fig. S5I). The protein levels of HA-tagged-Nfe2l2b$^{\Delta1/\Delta1}$ were reduced by 96% compared with those in Nfe2l2b^{wt} (P<0.0001) (Fig. S5J). Homozygous *nfe2l2b*$^{\Delta1/\Delta1}$ mutants survived to adulthood, with no general difference in appearance compared with their WT siblings (Fig. 5M). However, compensatory disruption of *nfe2l2b* through the generation of *aars1*$^{cq71/cq71}$;*nfe2l2b*$^{\Delta1/\Delta1}$ mutant larvae attenuated the phenotypes of increased $TUNEL^+$ signals and brain atrophy in the *aars1*$^{cq71/cq71}$ mutants (Fig. 5N,O). Intriguingly, the phenotypes of the neural populations, reflected by $Sox2^+$, *neurod1*$^+$ and even *oligo2*$^+$ cells, were significantly recovered in the *aars1*$^{cq71/cq71}$;*nfe2l2b*$^{\Delta1/\Delta1}$ mutants to the levels in either the WT siblings or *nfe2l2b*$^{\Delta1/\Delta1}$ embryos (Fig. 5P-R). Taken together, these results indicate that Nfe2l2b serves as a sufficient downstream player of Perk signaling via transcript control by Chop and activity manipulation by Perk to regulate NPC survival and neurogenesis in embryonic zebrafish (Fig. 5S).

p53 is a direct target of Nfe2l2b in mastering neuronal survival

NRF2 is a transcription factor (Fernández-Millán et al., 2016), the targets of which we dissected. *p53* was selected as a candidate based on the predicted Nrf2-binding site (GTAACAAAG) in its promoter

Development (2022) 149, dev200342. doi:10.1242/dev.200342

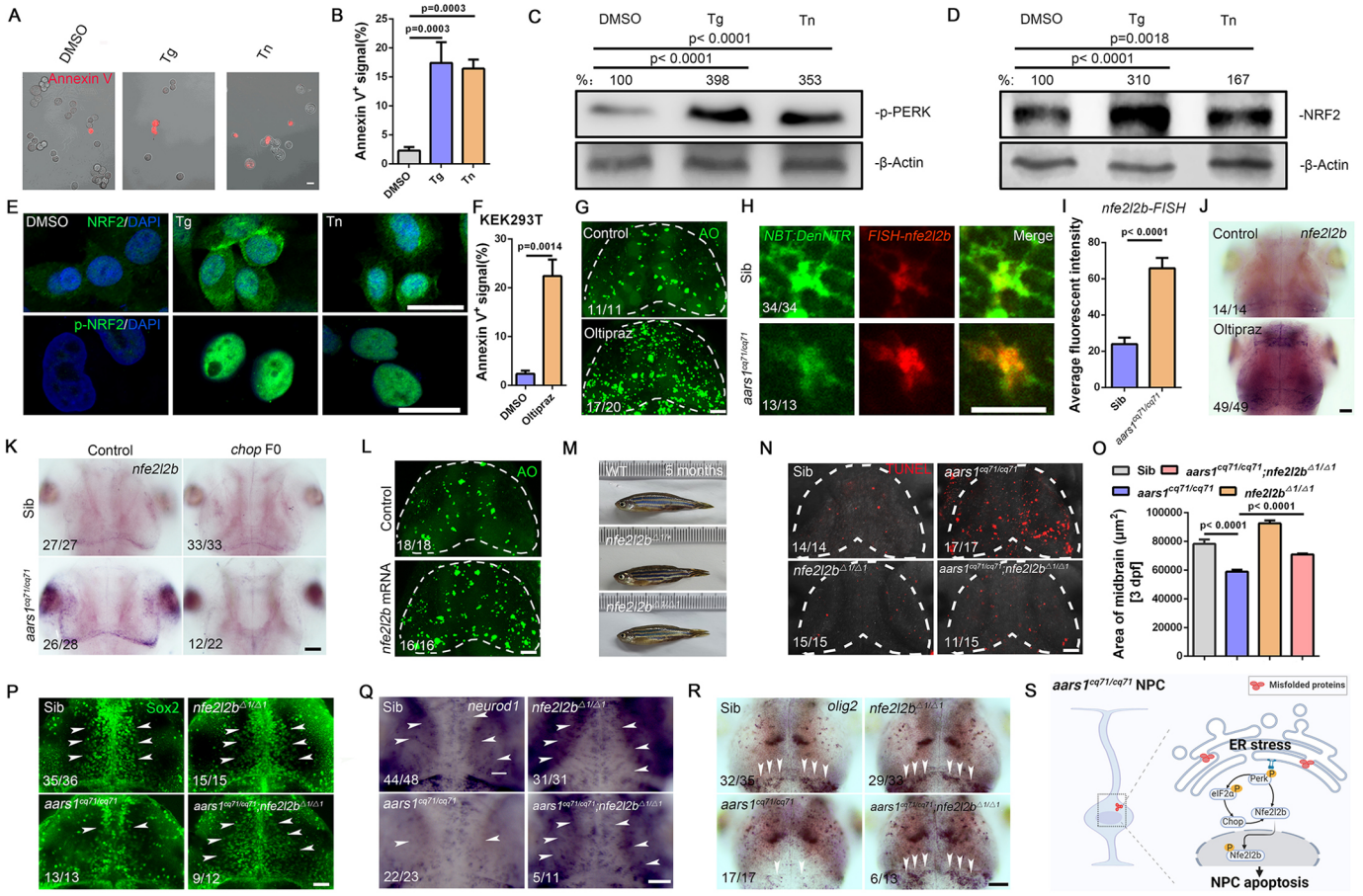

Fig. 5. *nfe2l2b* functions downstream of Perk in *aars1*$^{cq71/cq71}$ mutants. (A,B) Representative images (A) and quantification (B) of annexin V$^+$ signals in HEK293T cells (mean±s.e.m.; DMSO, 2.29±0.64 *n*=7; Tg, 17.43±3.55 *n*=7; Tn, 16.44±1.56 *n*=9; two independent clutches; one-way ANOVA). (C,D) Western blot of p-PERK (C) and NRF2 (D). The protein levels of p-PERK increased by 298% (*P*<0.0001) and 253% (*P*<0.0001) in the Tg and Tn groups, respectively. The protein levels of NRF2 increased by 210% (*P*<0.0001) and 67% (*P*=0.0018) in the Tg and Tn groups, respectively. (E) Immunofluorescent images of NRF2 (top row) and p-NRF2 (bottom row). (F) Quantification of annexin V$^+$ signals in HEK293T cells (mean±s.e.m.; DMSO, 2.36±0.66 *n*=7; oltipraz, 22.41±3.38 *n*=18; two independent clutches; unpaired two-tailed Student's *t*-test). (G) Fluorescent images of AO$^+$ signals in the zebrafish midbrains (white dashed lines). (H,I) Representative images (H) and average fluorescence intensity quantification (I) of NBT-DenNTR (green) and *nfe2l2b* transcript (red) in the midbrains (mean±s.e.m.; sibling, 23.92±3.66 *n*=18; *aars1*$^{cq71/cq71}$, 65.86±5.65 *n*=20; two independent clutches; unpaired two-tailed Student's *t*-test). (J,K) WISH images of *nfe2l2b* in the brains. (L) Fluorescent images of AO$^+$ signals in the midbrains (white dashed lines). (M) The globe appearance of 5-month-old WT, *nfe2l2b*$^{\Delta1/+}$ and *nfe2l2b*$^{\Delta1/\Delta1}$ mutant male zebrafish. (N) Immunofluorescent images of TUNEL$^+$ signals in the midbrains (white dashed lines). (O) Quantification of midbrain size (mean±s.e.m.; sibling, 78,201.27±3053.39 *n*=12; *aars1*$^{cq71/cq71}$, 58,860.49±1452.75 *n*=13; *nfe2l2b*$^{\Delta1/\Delta1}$, 92,589.72±1977.14 *n*=12; *aars1*$^{cq71/cq71}$ and *nfe2l2b*$^{\Delta1/\Delta1}$, 70,933.32±659.96 *n*=20; two independent clutches; one-way ANOVA). (P-R) Immunofluorescent staining images of Sox2 (P), and WISH images of *neurod1* (Q) and *olig2* (R), in the brains. The arrowheads indicate the signals. (S) Schematic illustration of Nfe2l2b in regulating NPC apoptosis in *aars1*$^{cq71/cq71}$ mutants. Scale bars: 20 μm.

sequence element (Fig. 6A). Chromatin immunoprecipitation (ChIP) and luciferase assays were then performed. The ChIP results indicated that Nfe2l2b is bound to the element (GTAACAAAG) located at the −639 site of the *p53* promoter *in vivo* (Fig. 6B). Luciferase activity increased ∼3.5-fold after addition of the vectors harboring this element compared with the control (Fig. 6C). However, mutating this coding sequence (CDS) caused an obvious reduction in luciferase activity by ∼2-fold (Fig. 6C). Meanwhile, the WISH results showed that the *p53*$^+$ signals were markedly decreased in the *nfe2l2b*$^{\Delta1/\Delta1}$ mutant brains, but significantly increased upon *nfe2l2b* mRNA injection (Fig. 6D,E). Overexpression of *nfe2l2b* mRNA in *Tg(NBT:DenNTR)* embryos followed by triple fluorescent labeling revealed that *p53*$^+$ signals were ectopically detected in NBT-DenNTR$^+$ cells, which colocalized with *nfe2l2b* and displayed TUNEL$^+$ signals (Fig. 6F,G). Additionally, P53 protein levels increased markedly in cultured HEK293T cells treated with Tg in a dose-dependent manner (Fig. S6A). Similarly, the *p53* transcript levels were significantly increased in NBT-DenNTR$^+$ cells in the *aars1*$^{cq71/cq71}$ mutant brains but decreased markedly upon knocking out either *nfe2l2b* or *chop* (Fig. 6H-J, Fig. S6B). These data indicate that *p53* is a direct target of Nrf2. We then generated a *Tg(hsp70:p53)* line in which full-length *p53* is driven by the *hsp70* promoter (Wu and Wang, 2020) (Fig. S6C). To facilitate screening, the lens protein Cryaa-Cerulean-BGHpA element was inserted in reverse sequence. This allowed us to temporally induce *p53* expression at the desired time points via heating (Wu and Wang, 2020). We validated the successful overexpression of *p53* transcripts based on the appearance of Cerulean$^+$ signals in the retina and *p53*$^+$ signals in the body (Fig. S6D,E). Appearance of AO$^+$ signals in the brains and significantly decreased midbrain size were observed in heat-shocked 3 dpf *Tg(hsp70:p53)* embryos (Fig. S6F,G). In contrast, transient knockdown of *p53* in *aars1*$^{cq71/cq71}$ embryos by *p53* morpholinos (MOs) markedly attenuated the phenotypes of AO$^+$

Development (2022) 149, dev200342. doi:10.1242/dev.200342

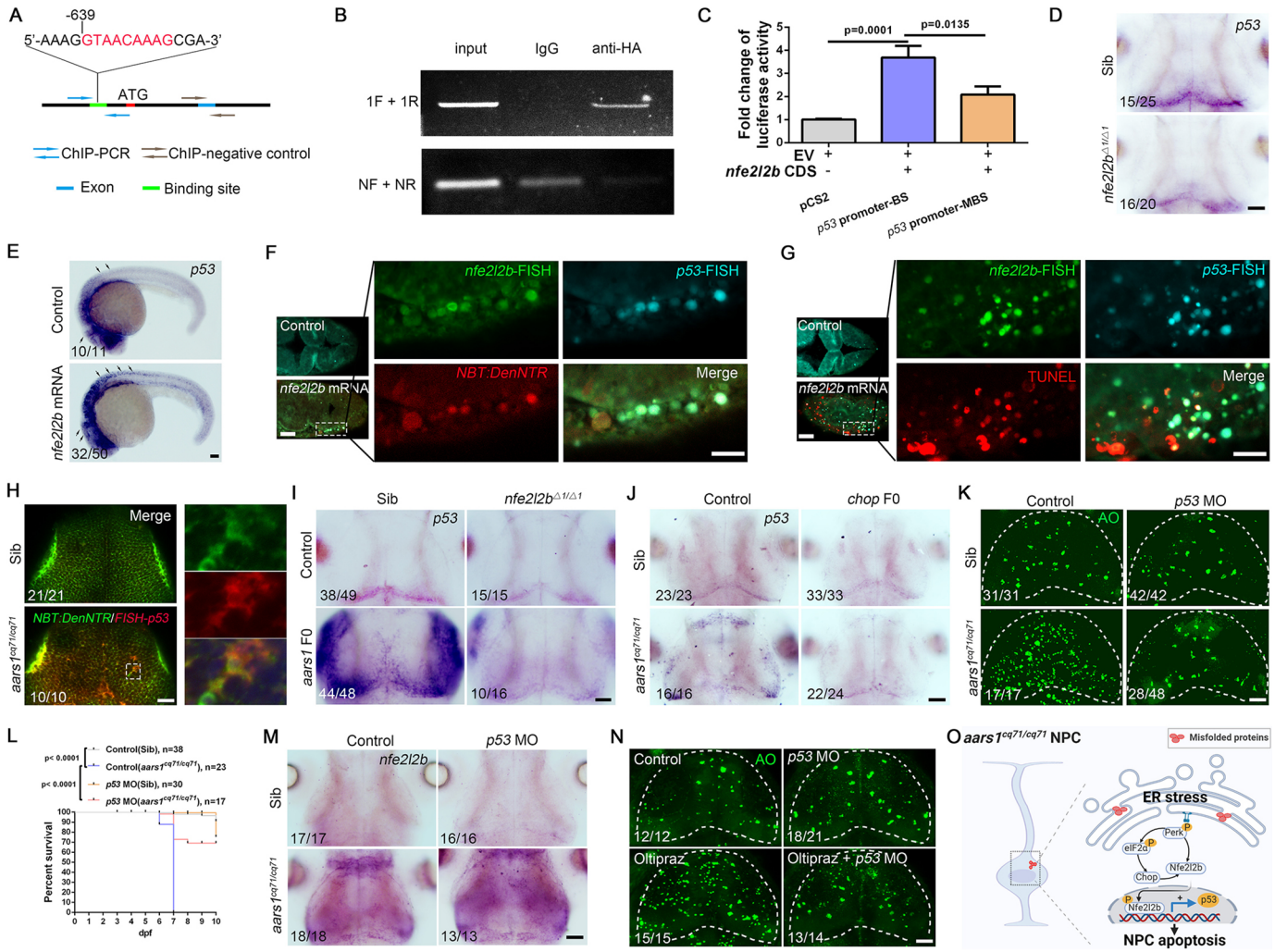

Fig. 6. *p53* is a direct target of *nfe2l2b* in neural apoptosis. (A) Schematic of the *p53* promoter. Chromatin immunoprecipitation (ChIP)-PCR analysis of the Nfe2l2b-binding site (green) in the *p53* promoter. Blue arrows indicate the ChIP-PCR; gray arrows indicate the ChIP-negative control. Blue rectangle indicates the selected exon in *p53*. (B) ChIP-PCR results. IgG, immunoglobulin G; 1F, forward primers; 1R, reverse primers; NF, negative forward primers; NR, negative reverse primers. (C) Luciferase activities of the plasmids containing different promoter elements (mean±s.e.m.; pCS2, 1.00±0.02 *n*=6; *p53* promoter-BS, 3.69±0.20 *n*=6; *p53* promoter-MBS, 2.08±0.15 *n*=6; two independent clutches; one-way ANOVA). CDS, coding sequence, EV, pCS2 vector. (D,E) WISH images of *p53* in the brains (D) and embryos (E). The arrows indicate the signals. (F,G) Immunofluorescent images of triple staining of *nfe2l2b* (green) and *p53* (turquoise) transcripts with *NBT:DenNTR* (F) or TUNEL (G) after injecting *nfe2l2b* mRNA. The left images indicate the midbrain regions, and the white dashed lines highlight the regions of enlarged images on the right. (H) Immunofluorescent images of double staining of *NBT:DenNTR* (green) and *p53* (red) transcript in the midbrains. The right column contains enlarged images of the boxed region on the left. (I,J) WISH images of *p53* in the brains. (K) Fluorescent images of AO^+ signals in the midbrains (white dashed lines). (L) Kaplan–Meier survival analysis (log-rank/Mantel–Cox statistic). (M) WISH images of *nfe2l2b* in the brains. (N) Fluorescent images of AO^+ signals in the midbrains (white dashed lines). (O) Schematic illustration of *p53* as a direct executor of Nfe2l2b in controlling NPC apoptosis in *aars1*$^{cq71/cq71}$ mutants. Scale bars: 20 µm.

signals, enlarging the pool of NBT-DenNTR$^+$ cells and midbrain volume (Fig. 6K, Fig. S6H,I). These *p53* MO-treated *aars1*$^{cq71/cq71}$ embryos survived much longer than their untreated controls (Fig. 6L); however, no notable *nfe2l2b* transcript alterations were observed simultaneously (Fig. 6M), further supporting the epistatic effect of Nfe2l2b on *p53*. Similarly, we observed that *p53* knockdown significantly decreased cell death in oltipraz-treated embryos (Fig. 6N). Taken together, these results showed that *p53* acts as an executor of Nfe2l2b in the regulation of neuronal survival and neurogenesis in embryonic zebrafish (Fig. 6O).

Neuronal apoptosis of defective threonyl-tRNA synthetase via the same Perk–Nrf2 axis

We then investigated whether other aminoacyl-tRNA synthetases regulated neuronal survival and neurogenesis via the same Perk–Nrf2 axis. scRNA-seq data revealed the enrichment of several ARS members in various neuronal subpopulations, in which *tars1* was highly expressed in clusters 4 and 5 (Fig. 7A). We characterized the phenotype of *tars1*$^{cq16/cq16}$ mutants (Cao et al., 2016). *tars1*$^{cq16/cq16}$ mutant embryos presented a notably smaller head than that of their WT siblings and a curled-up tail (Fig. 7B). The AO^+ and $TUNEL^+$ signals increased dramatically, but the numbers of NeuN$^+$ (Rbfox3a$^+$) cells and transcript levels of *map2* and *tuba1b* were substantially reduced, in *tars1*$^{cq16/cq16}$ mutants relative to their WT siblings (Fig. 7C-E). These data indicate increased neuronal apoptosis and failed neurogenesis in *tars1*$^{cq16/cq16}$ mutants. The UPR of ER stress signaling was initiated in *tars1*$^{cq16/cq16}$ mutants, as indicated by elevated transcript levels of *bip* and *chop* and an obvious attenuation of cell apoptosis upon CHX application (Fig. 7F,G). Similar to in the

Development (2022) 149, dev200342. doi:10.1242/dev.200342

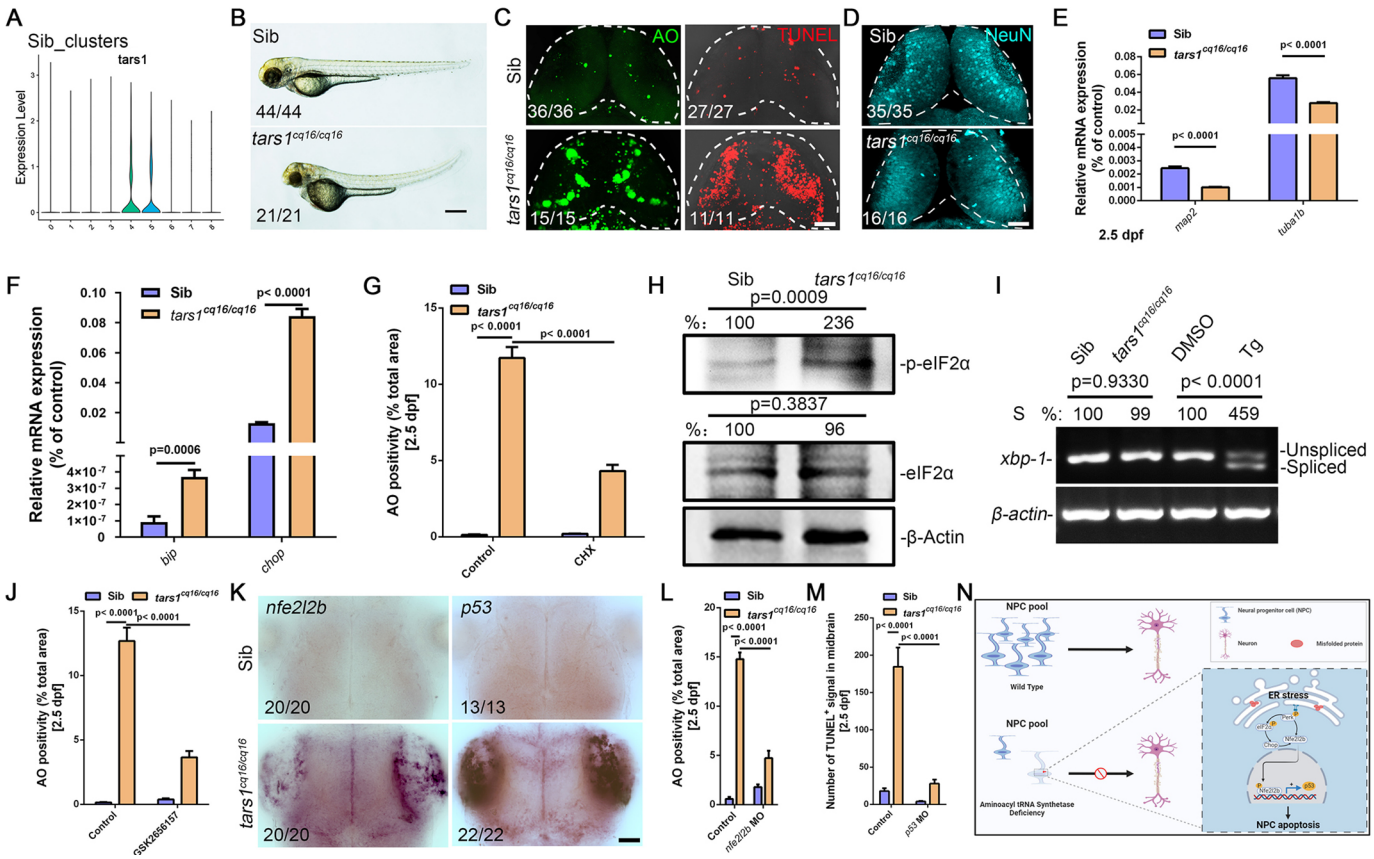

Fig. 7. The Perk–Nrf2–P53 axis is similarly utilized in *tars1*$^{cq16/cq16}$ mutants as in *aars1cq71/cq71* mutants. (A) Violin plot of *tars1* expression in nine neural cell clusters. (B) Brightfield morphological images. (C) Fluorescent images of AO (green) and TUNEL (red) staining in the midbrains (white dashed lines). (D) Fluorescent images of NeuN (turquoise) in the midbrains (white dashed lines). (E,F) qRT-PCR (mean±s.e.m.; *n*=6 in each group; two independent clutches; unpaired two-tailed Student's *t*-test) of *map2* and *tuba1b* (E) and *bip* and *chop* (F). (G) Quantification of AO$^+$ signals (mean±s.e.m.; control: sibling, 0.13±0.03 *n*=12; *tars1*$^{cq16/cq16}$, 11.72±0.72 *n*=15; CHX: sibling, 0.20±0.02 *n*=12; *tars1*$^{cq16/cq16}$, 4.32±0.40 *n*=15; two independent clutches; two-way ANOVA). (H) Western blot of p-eIF2α and eIF2α. The protein levels of p-eIF2α increased by 136% (*P*=0.0009) in the *tars1*$^{cq16/cq16}$ mutants compared with those in siblings. (I) *xbp1* splicing. Treatment of 24 hpf WT embryos with Tg for 1 h is used as a positive control. S, spliced *xbp1*. The levels of spliced *xbp1* increased by 359% (*P*<0.0001) in the Tg group compared with those in the controls. (J) Quantification of AO$^+$ signals (mean±s.e.m.; control: sibling, 0.14±0.03 *n*=13; *tars1*$^{cq16/cq16}$, 12.67±1.04 *n*=12; GSK2656157: sibling, 0.38±0.08 *n*=13; *tars1*$^{cq16/cq16}$, 3.65±0.49 *n*=12; two independent clutches; two-way ANOVA). (K) WISH images of *nfe2l2b* and *p53* in the brains. (L,M) Quantification of AO$^+$ (L) (mean±s.e.m.; control: sibling, 0.59±0.20 *n*=13; *tars1*$^{cq16/cq16}$, 14.78±0.67 *n*=13; *nfe2l2b* morpholino (MO): sibling, 1.78±0.27 *n*=13; *tars1*$^{cq16/cq16}$, 4.72±0.75 *n*=13; two independent clutches; two-way ANOVA) and TUNEL$^+$ signals (M) (mean±s.e.m.; control: sibling, 17.79±4.07 *n*=14; *tars1*$^{cq16/cq16}$, 184.50±25.83 *n*=11; *p53* MO: sibling, 3.88±0.89 *n*=14; *tars1*$^{cq16/cq16}$, 27.81±5.62 *n*=11; two independent clutches; two-way ANOVA). (N) Schematic diagram of our working model. Scale bars: 1000 µm (B); 20 µm (C,D,K).

aars1$^{cq71/cq71}$ mutant, the Perk pathway was selectively activated. The protein levels of p-eIF2α were increased by 136% in *tars1*$^{cq16/cq16}$ mutants compared with WT siblings (*P*=0.0009) (Fig. 7H). However, the splice of *xbp1* transcript failed in the *tars1*$^{cq16/cq16}$ embryos (Fig. 7I). Concordantly, interfering with Perk functions in *tars1*$^{cq16/cq16}$ embryos by GSK2656157 treatment remarkably reduced the aggregated AO$^+$ signals (Fig. 7J). Likewise, the expression levels of *nfe2l2b* and *p53* were increased in *tars1*$^{cq16/cq16}$ mutant brains compared with those in the brains of their WT siblings (Fig. 7K). Transient interference with the functions of *nfe2l2b* or *p53* by MO administration significantly repressed the AO$^+$ and TUNEL$^+$ signals in the *tars1*$^{cq16/cq16}$ mutant midbrain (Fig. 7L,M), implying that *tars1* deficiency caused neuronal apoptosis through a similar Perk–Nrf2 pathway. Taken together, our study results demonstrated that abrogated protein metabolism caused by tRNA synthetase deficiency led to accelerated apoptosis of NPCs and compromised neurogenesis, as determined by Nrf2 and its target *p53*. Nrf2 function was doubly controlled. *nfe2l2b* transcript was regulated by Chop, with nuclear activation being promoted by Perk phosphorylation (Fig. 7N).

DISCUSSION

In the present study, we identified a recessive *aars1*$^{cq71/cq71}$ mutant zebrafish allele. *aars1*$^{cq71/cq71}$ mutant harbored a point mutation that led to a premature stop codon in the amino acid activation domain and generated a rapidly decayed truncated Aars1 protein. The abrogation of Aars1 functions in the present *aars1*$^{cq71/cq71}$ null mutant zebrafish was initially anticipated to cause a failure in protein synthesis; however, aggregated loads of ubiquitylated proteins and intensive ER stress were observed in the *aars1*$^{cq71/cq71}$ mutant brains. This result implied that other tRNA synthetases had a compensatory function, resulting in the production of large amounts of misfolded proteins. Indeed, the transcripts of *nars1*, *tars1*, *eprs1*, *mars1*, *yars1*, *iars1*, *hars1*, *kars1*, *sars1*, *fars1* and *gars1* were markedly increased in the *aars1*$^{cq71/cq71}$ mutant brains, based on the results of scRNA-seq and WISH (Fig. S6J,K).

scRNA-seq analysis revealed intensive enrichment of *aars1* in NPCs, particularly in the primary stages. This different pattern of *aars1* transcription from that of the other members of the ARS family points to a special and/or unique role of *aars1* in harnessing the signatures of NPCs during embryonic neurogenesis.

Development (2022) 149, dev200342. doi:10.1242/dev.200342

Concordantly, significant apoptosis of NPCs was observed in both the ENU screening and CRISPR/Cas9-created *aars1* mutant zebrafish alleles, and this phenotype could be rescued by human *AARS1*, highlighting the solid and conserved roles of *aars1*. Interestingly, scRNA-seq analysis revealed a remarkably enlarged pool of neuronal progenitors in 2 dpf *aars1*$^{cq71/cq71}$ mutant brains before pronounced cell apoptosis. These data implied the blockage of differentiation and maintenance of quiescence when progenitors lacked proper protein supplementation. The maintenance of progenitor characteristics is controlled by a set of factors, and Notch activity is a key clue in this situation (Alunni et al., 2013). Consistently, our sequencing data indicated Notch signaling activation (Fig. S6L), but the reasons behind its activation upon compromised *aars1* functions were still elusive. Whether and how Notch signaling is involved in ER stress and neuronal apoptosis remains an open question.

In the *aars1*$^{cq71/cq71}$ and *tars1*$^{cq16/cq16}$ mutants, intensive UPR reactions specifically activated the Perk signaling branch, causing a dramatic increase in apoptotic cells. PERK activation occurs when the UPR is beyond tolerance or adaptation, eventually leading to apoptosis through mitochondrial signaling (Ansari et al., 2018). QRICH1 was identified as an interesting factor downstream of the PERK–eIF2 axis as a distinct arm of ATF4 to determine cell fate through proteostasis modulation (You et al., 2021). However, the key executive targets of the *atf4–chop* axis in cell death are unclear. Taking advantage of this genetic manipulation, we recognized that *nfe2l2b*, a paralog of *Nfe2l2*, is an essential mediator of Perk signaling that regulates cell apoptosis upon UPR.

In previous studies, NRF2 was found to be a transcriptional factor that plays a critical role in defense against electrophiles and oxidative stress (Kawai et al., 2011). However, some reports have shown that ER stress activates NRF2 activity, whereas others have opposed these opinions (Chang et al., 2018; Kang et al., 2019). Interestingly, two paralogs of *Nfe2l2* have been found in zebrafish. The *nfe2l2a* paralog was closer to *Nfe2l2* than *nfe2l2b*. A recent zebrafish study demonstrated that *nfe2l2a* transcript was detected in the brain and liver, and its activation ameliorated mild ER stress in the *pmm2* mutant liver (Mukaigasa et al., 2018). However, we did not observe a notable increase in the *nfe2l2a* paralog in the *aars1*$^{cq71/cq71}$ mutants, and its forced supplementation had limited effects. In contrast, *nfe2l2b* appeared in the midbrain, presenting marked elevation in its transcript level in the *aars1*$^{cq71/cq71}$ mutants. Unlike for the *nfe2l2a* paralog, oversupply of *nfe2l2b* induced cell apoptosis. Conversely, interfering with *nfe2l2b* in *aars1*$^{cq71/cq71}$; *nfe2l2*$^{\Delta 1/\Delta 1}$ mutants rescued the extensive neuronal apoptosis induced by ER stress in *aars1*$^{cq71/cq71}$ mutants. The distinct effects of *nfe2l2a* and *nfe2l2b* on zebrafish neuronal survival suggest a diversity of Nrf2 functions in a context-dependent manner. This alluded to a possible interpretation of the debate regarding the NRF2 response to ER stress. It is a common result that fish harbor duplicated forms of a plethora of factors. Thus, another possibility is that *nfe2l2b* was a unique duplicated factor of Nrf2 acquired by zebrafish during evolution. However, the pro-apoptotic role of *nfe2l2b* extends the understanding of crucial molecules in ER stress.

The target genes of NRF2 in ER stress are limited. A recent study has documented the interaction of NRF2 with P53 in promoting cancer cell death (Kang et al., 2019). Our study indicated that *p53* was a direct target of Nrf2 and its transcript was significantly reduced in *nfe2l2b*$^{\Delta 1/\Delta 1}$ mutants but increased upon overexpression of *nfe2l2b*, in which p-NRF2 entered the nucleus to directly increase the levels of *p53* to induce cell apoptosis. These data are in contrast to a previous report that an increase in *p53* level was observed using *nfe2l2b* MO (Timme-Laragy et al., 2012). We believe that the difference was probably caused by the different methods and tissues used in the two studies. The present study examined the *p53* transcripts in *nfe2l2b*$^{+}$ cells using both WISH and FISH, in contrast to the previous bulk qPCR analysis of whole embryos (Timme-Laragy et al., 2012). Furthermore, this hypothesis supports organ sensitivity to NRF2. The homozygous *nfe2l2b*$^{\Delta 1/\Delta 1}$ mutants were able to survive to adulthood and were comparable to the WT siblings, suggesting the non-essential role of *nfe2l2b* in organ development. However, an obvious reduction in the *p53* transcripts was observed in the *nfe2l2b*$^{\Delta 1/\Delta 1}$ mutant midbrain. Considering the wide spectrum of the effects of decreased *p53*, further studies should focus on the neuronal phenotypes in the *nfe2l2b*$^{\Delta 1/\Delta 1}$ mutants, especially in adult animals. Overall, our study extends the understanding of the regulatory mechanisms of UPR caused by compromised tRNA synthesis during neurogenesis. Misfolded proteins have been found to activate Perk signaling, leading to increased apoptosis of NPCs and termination of neurogenesis via the Nrf2–p53 axis. Nrf2 is a critical factor in the determination of cell fate and may be considered a target to attenuate neurodegenerative disorders with defective tRNA synthesis.

MATERIALS AND METHODS

Zebrafish and cell line

Complete information on the zebrafish (*Danio rerio*) strains is provided in Table S2. All experimental protocols were approved by the School of Life Sciences, Southwest University (Chongqing, China). The methods were approved by the guidelines. Fish were raised at 28.5°C under a 14 h light/10 h dark cycle. Embryos were obtained after natural spawning and were put in E3 buffer with 0.003% 1-phenyl-2-thiourea (PTU; Sigma) to prevent pigment formation. The zebrafish facility and study were approved by the Ethics Committee of the College of Life Science, Southwest University. The HEK293T cell line (see Table S2) was cultured following a standard protocol. The medium contained high-glucose Dulbecco's modified Eagle medium (DMEM) with glutamine and sodium pyruvate (Biological Industries), 10% fetal bovine serum (Biological Industries), 1% L-glutamine (Beyotime), 1 µg/ml Mycoplasma Removal Agent Plus (Beyotime) and 1% Penicillin-Streptomycin-Amphotericin B Solution (Beyotime). The cells were grown in an incubator (Shanghai Yiheng Technology) following a standard protocol.

ENU mutagenesis and positional cloning

ENU mutagenesis and positional cloning were performed as previously described (Trevarrow, 2011). The genetic mapping strain *ENU*/WIK was created by crossing heterozygous *ENU* mutant with WT WIK zebrafish. WT and mutant embryos were phenotypically collected from pairwise mating of heterozygous *ENU*/WIK zebrafish. The Mut$^{cq71/cq71}$ embryos presented an obvious reduction of neuronal markers at 2.5-3 dpf. We first located the mutation to linkage group (LG)18 by bulked segregation analysis, which indicated a close linkage of the mutant pools with the sequence-length polymorphism (SSLP) markers in LG18. SSLP markers and SNPs were used to perform the fine mapping to narrow the genetic interval. The cDNA of candidate genes was cloned and sequenced from pooled mutants, Finally, a point mutation in exon 5 of *aars1* gene (Ensembl: ENSDARG00000069142) was identified in Mut$^{cq71/cq71}$ embryos based on the sequencing data.

Genetic manipulation

aars1$^{\Delta 10/\Delta 10}$ and *nfe2l2b*$^{\Delta 1/\Delta 1}$ mutant alleles were generated by the CRISPR/Cas9 system (Chang et al., 2013). The gRNAs targeting the 5′-GGGA-CGGGTCAATGGTGTTCAGG-3′ in *aars1* exon 4, and 5′-TGGATG-TCTCCGGCAGAGGG-3′ in *nfe2l2b* exon 2, were *in vitro* synthesized by a mMESSAGE mMACHINE T7 transcription kit (Thermo Fisher Scientific). Cas9 protein was mixed with gRNA according to the manufacturer's instruction (Biolabs). The mixture was injected into the fertilized embryos at one-cell stage. The *aars1*$^{\Delta 10/\Delta 10}$ and *nfe2l2b*$^{\Delta 1/\Delta 1}$ mutant alleles were

Development (2022) 149, dev200342. doi:10.1242/dev.200342

obtained by DNA sequencing. To construct the *pT2AL2-NBT:aars1;cryaa:cerulean* plasmid, the full length of the *aars1*^{202} cDNA fragment was amplified and subcloned into the *pT2AL2-NBT;cryaa:cerulean* backbone (Tilton and Tanguay, 2008; Wu et al., 2018). Similarly, to construct *Tg(hsp70:p53)* plasmids, specific primers (Table S1) were used to amplify its cDNA sequence and clone into the pTol2-*hsp70* backbone (Wu and Wang, 2020). To facilitate screening, a Cryaa-Cerulean-BGHpA element (Hesselson et al., 2009) was inserted reversely. The *pT2AL2-NBT:aars1;cryaa:cerulean* constructs (30 ng/µl) containing Tol2 transposase mRNA (250 ng/µl) were co-injected into the WT embryos at one-cell stage to build the F0 founders. The stable transgenic lines were recovered in the F1 generation based on the appearance of *cerulean*$^{+}$ signals in the eyes and the same WISH patterns of *aars1* as that of *NBT*. The *Tg(hsp70:p53;cryaa:cerulean)* and *Tg(NBT:DenNTR)* heritable zebrafish transgenic lines were generated by the same methods.

Heat shock assay

Embryos with *Tg(hsp70:p53)* transgenic background were heated to 38.5°C for 40 min and then incubated at 28.5°C. The efficiency of *p53* expression after heat shock was verified by fluorescence signals in the eye and presentation of *p53* by WISH.

Staining assays

RNA probes were synthesized by a DIG RNA Labeling Kit T3/T7/SP6 (Roche). WISH and FISH experiments were performed as described previously (He et al., 2020; Huang et al., 2019). TUNEL staining was performed using an In Situ Cell Death Detection Kit and TMR Red Kit (Roche) following the manufacturer's instructions or as reported previously (Lei et al., 2017). AO staining was performed as described (Thompson et al., 2015). Briefly, zebrafish embryos were incubated with 10 µg/ml AO solution in the dark at 28.5°C for 40 min. They were then observed by a Carl Zeiss Discovery V20 microscope. Immunofluorescence staining of zebrafish embryos was performed following standard protocols (Zhao et al., 2018). Briefly, embryos of the desired stages were fixed by 4% paraformaldehyde (4°C, overnight). The embryos were then co-incubated with the primary antibody (Table S2) at 4°C overnight. Afterwards, the samples were rinsed with PBDT (phosphate buffer containing 1% DMSO and 0.02% Tween 20) and then stained with Alexa Fluor 488/555/647-conjugated secondary antibodies (Table S2). The WISH images were captured by a Carl Zeiss Discovery V20 microscope. The immunofluorescence staining images were photographed by LSM700 or LSM880 confocal microscopes.

Behavioral recording

The behavioral study was performed according to a previous description (Palmér et al., 2017). Individual zebrafish larvae were placed in a plate containing 1 ml egg water. To record the movement of spontaneous swimming behavior, larvae were adaptive for 5 min, and their behaviors were then captured for 5 min by a scan camera (Basler, model ACA1300-60 GC). Their behaviors after light–dark and needle stimulation were monitored following reported studies (Marquez-Legorreta et al., 2020; Sztal et al., 2016). Briefly, to perform the light–dark stimulation experiment, the larvae were first adapted in a recording box with light for 30 min. Then, the light was turned off for 5 min and then turned on for another 5 min. The track of larvae in the 10 min light–dark cycle was monitored by an area scan camera. To conduct the needle stimulation, a sterilized syringe needle was used to touch the larval head, and the area scan camera was used to capture the swimming track for 3 min. All the imaging data were analyzed by the Ethovision XT15 animal tracking system (Noldus). The distance and movement speed were calculated accordingly.

Timelapse imaging

Ca^{2+} activities of neurons were monitored in *Tg(HuC:GCaMP6s)* embryos. Embryos were immobilized in 1% low-melting point agarose in a 35 mm glass-bottom dish. *In vivo* uninterrupted time-series Ca^{2+} imaging experiments were performed with scanning (1.2 Hz at an excitation of 488 nm) under an LSM880 confocal microscope (Carl Zeiss), and the resolution was 512×512 pixels. The data were extracted by ZEN2012 software, and the movies were created by Corel Video Studio.

Annexin V staining

Annexin V staining was performed following previous instructions (She et al., 2018). Briefly, Alexa Fluor 488-conjugated Annexin V (Molecular Probes) was mixed with 1× binding buffer at a ratio of 1:1 (BioVision). The mixtures were loaded into the midbrain gaps of 3 dpf zebrafish, which were then incubated in the dark for 1.5 h. Similarly, after HEK293T cells were treated with 500 µl trypsin solution for 1 min, the cells were collected and washed twice with pre-cooled PBS. A mixture of 100 µl 1× binding buffer and 5 µl annexin V-FITC were added to the preparations of 1×10^{6} cells. These cells were then incubated (37°C) in the dark for 5 min. The signals were visualized by a LSM700 confocal microscope.

Blastomere cell transplantation

Cell transplantation was performed as previously described (Zou and Wei, 2010). Approximately 30-50 blastomere cells were drawn from 1000-cell stage WT and *aars1* RNP F0 donors with *Tg(NBT:DenNTR)* background and loaded into needles. The blastomere cell-filled needles were injected into the animal pole of 1000-cell stage host embryos (*aars1*$^{cq71/cq71}$ or siblings). The cells were slowly released by a micromanipulator (Eppendorf CellTram 4r Oil).

Transmission electron microscopy (TEM)

TEM was conducted by Wuhan Servicebio Technology. We prepared the samples according to their instructions. Briefly, the anaesthetized 3 and 5 dpf zebrafish larvae were placed in pre-cooled 1× PBS, and the midbrains were microdissected using 0.33 mm micro-fine sterile needles. The samples were fixed in the electron microscope fixation solution for 2 h. They were then moved to 1% OsO_4 in 0.1 M phosphate buffer (PB) (pH 7.4) in the dark at room temperature for 2 h. After removing OsO_4, the tissues were rinsed with 0.1 M PB (pH 7.4) for 15 min, repeated three times. Fixed embryos were gradually dehydrated with ethanol and embedded individually into resin blocks. The resin blocks were cut to 60-80 nm thickness by an ultramicrotome (Leica UC7). The tissues were placed onto 150 mesh cuprum grids with formvar film, and then stained with 2% uranium acetate saturated alcohol solution and 2.6% lead citrate. Images were acquired using a Hitachi HT7800/HT7700 TEM.

Western blotting

Western blotting was performed as described previously (Zhao et al., 2018). Proteins were purified using cell lysis buffer (Beyotime). Subsequently, the membranes were blocked in Tris-buffered saline with 0.5% Tween 20 (TBST) containing 5% fat-free milk at 37°C for 1 h. The samples were then incubated with primary antibodies (Table S2), which were diluted by QuickBlock™ buffer (Beyotime) at 4°C overnight. After incubating with corresponding secondary antibodies (Table S2), the specific bands were detected by an Odyssey FC two-color infrared laser imaging system (LI-COR).

Vector construction and chemical treatment

The fragments of WT and mutated CDS of *aars1* were amplified by primers (Table S1). They were subcloned into a pCS2+ vector to synthesize mRNA using a mMESSAGEmMACHINE™ SP6 kit (Roche). *chop* and *nfe2l2b* mRNA were prepared by the same method. To perform the ChIP and luciferase experiments, we used a standard protocol to perform site-directed mutagenesis (Huang et al., 2019). Briefly, the primers were designed on both sides of the mutation sites, and 50 µl PCR reactions contained 100 ng template, 2 µl primer (F/R), 1 µl dNTPs, 1 µl fast-Pfu DNA polymerase and 5 µl reaction buffer. Each amplification cycle consisted of 95°C for 20 s, 50°C for 30 s and 68°C for 10 min. After that, the PCR products were treated with 1 µl DpnI (15 µl products) at 80°C for 10 min. They were then analyzed by agarose gel electrophoresis, and finally transformed into *Escherichia coli DH5α* by heat shock. The plasmids were isolated by a Miniprep Kit (Axygen) and then verified by sequencing. To perform chemical treatment, 1.5 dpf zebrafish embryos were incubated with GSK2656157 (65 µM), Tg (5 µM), Tn (1 µM), CHX (50 µM), oltipraz (10 µM) and Ceapin-A7

Development (2022) 149, dev200342. doi:10.1242/dev.200342

(50 µM). The HEK293T cells at designated time points were cultured with Tg (0.5 µM or 1 µM), oltipraz (40 µM) and Tn (6 µM) for 24 h.

ChIP and reporter assay

ChIP assay was performed using 24 hpf embryos injected with HA-*nfe2l2b* mRNA. Because there was no Nfe2l2b-specific antibody for ChIP assay in zebrafish, we pulled down the target DNA fragments using antibody against HA. The eluted DNA (precipitated by anti-HA antibody) was assayed by PCR. The primers were designed according to the conserved Nfe2l2b-binding sites (Table S1). Non-specific primers and rabbit purified IgG were used as controls. The luciferase assays were performed using a Dual-Luciferase Reporter Assay System (Beyotime). The luciferase activity was measured by a GloMax 20/20 luminometer (Promega) according to the manufacturer's instructions. The −2.6 kb p53 promoter was amplified by the primers (Table S1) and cloned into a pGL3-basic vector (Promega). The p53-binding sites were mutated by site-directed mutagenesis using the designed site-specific oligonucleotide primers (Table S1). HEK293T cells were cultured in DMEM with 10% fetal bovine serum in 24-well plates. According to a standard protocol of Lipo8000™ Transfection Reagent (Beyotime), the plasmids (200 ng pGL3-p53 promoter, 200 ng pGL3-p53 promoter-MBS, 250 ng pCS2-nfe2l2b CDS, 250 ng pCS2 and 40 ng pRL-CMV) were transfected into cells and cultured for 36 h. Finally, the cells were harvested to perform luciferase assays using a Dual Luciferase Reporter Gene Assay Kit (Beyotime).

Phylogenetic analysis, homology analysis and model design

The genomic sequences of *nrf2* and *aars1* were acquired from the Ensembl database. The predicted zebrafish Nrf2 amino acid sequence was aligned with human (*Homo sapiens*) by the neighbor-joining method. The standard Kimura two-parameter model was used for the construction of phylogenetic tree using Molecular Evolution Genetics Analysis software (MEGA, version 5.1) (Tamura et al., 2011). The divergence was determined by the distance matrix method. The pairwise distance of Aars1 among zebrafish, chicken, human and house mouse was estimated (https://www.ebi.ac.uk/Tools/msa/clustalo/). The model diagram was created in biorender.com.

Quantitative RT-PCR

Quantitative RT-PCR (qRT-PCR) was carried out using total RNA isolated from the brains of *aars1*$^{cq71/cq71}$ or WT siblings according to a previous method (Wu et al., 2018). NBT-DenNTR^{+}, Sox2-GFP^{+}, Neurod1-EGFP^{+}, Olig2-DsRed2^{+} and Coro1a-DsRed^{+} cells were sorted by fluorescence-activated cell sorting (Moflo XDP, Beckman). Then, cDNA libraries were generated by a REPLI-g WTA Single Cell Kit (Qiagen). All data were obtained by a Roche light cycler 96 machine and the expression levels of *β-actin* or *ef1α* were used as the reference. Table S1 lists information on the qRT-PCR primers.

scRNA-seq

scRNA-seq was conducted by AccuraMed. The embryonic midbrains of 2 dpf *aars1*$^{cq71/cq71}$ and WT siblings were extracted under a stereomicroscope by syringes and needles. They were then dissected in the ice-cold Dulbecco's phosphate-buffered Saline (DPBS) and dissociated using a Papain Dissociation Kit (Worthington) according to the manufacturer's instruction (Tambalo et al., 2020). Subsequently, the samples were centrifuged at 200 ***g*** for 4 min and washed twice with 1 ml DPBS. Then, the cells were filtered through a 40 µM cell strainer and finally resuspended in DPBS. The single-cell suspension was promptly loaded on a 10× Chromium System and sent to AccuraMed. The 10× libraries were prepared as per the manufacturer's instructions. The raw sequencing data were processed by the Cell Ranger software with the default options. The reads were aligned to zebrafish transcriptome reference (ENSEMBL Zv10, release 91). The resulting matrices were used as input for the downstream analysis by Seurat.

Data analysis

The analyses on the UMI count matrix in the two datasets were performed using the R package Seurat (version 4.0.1) (Butler et al., 2018) following the standard workflow in the Satija laboratory webpage (https://satijalab.org). The *aars1*$^{cq71/cq71}$ and sibling datasets were merged using the Seurat function Merge Seurat (https://www.rdocumentation.org/packages/Seurat/versions/3.1.4/topics/merge.Assay) (Stuart et al., 2019). Initial quality control was performed by filtering out genes expressed in less than one cell. Gene selection for dimensional reduction was accomplished using the Seurat function Find Variable Genes (https://www.rdocumentation.org/packages/Seurat/versions/2.3.4/topics/FindVariableGenes). Following gene selection, all log-normalized expression values were scaled and centered using Scale Data (https://github.com/satijalab/seurat). Principal components were chosen according to the principal component analysis elbow plot, which ordered principal components from the highest to the lowest based on the percentage of variance explained by each principal component. Next, we performed clustering on each set of principal components and a second round of dimensional reduction using t-distributed stochastic neighbor embedding (t-SNE). Markers of each cell type were identified based on their significant differential gene expression (adjusted P<0.05) using the Seurat function Find All Markers (https://www.rdocumentation.org/packages/Seurat/versions/4.1.1/topics/FindAllMarkers). Clusters were annotated based on the expression datasets of these cluster-specific marker genes on ZFIN (https://zfin.org). Both datasets contained non-specific cell types that contained markers for glial (pharyngeal cells), retinal (cone bipolar cells) and erythrocyte cells were removed after the initial clustering. Following these stepwise processes, we finally obtained the purified data of each sample. To identify cell trajectories on pseudotime, the progenitor cells of Seurat object was converted to Monocle (Durruthy-Durruthy and Heller, 2015). We used the genes of canonical correlation analysis to order Monocle and defined the maximum component as 2.

GO-term analyses

GO analysis was performed in Database for Annotation, Visualization and Integrated Discovery (DAVID) (Xue et al., 2019). KEGG pathway analysis of highly differentially expressed genes was performed on progenitor cell clusters of *aars1*$^{cq71/cq71}$ versus WT siblings by the 'cluster Profiler' R package (Yu et al., 2012).

Statistics of AO signals, midbrain volume and survival ratio

The AO^{+} signals were quantified as described previously (Sidi et al., 2008). In brief, the images were analyzed by ImageJ software (National Institutes of Health, Bethesda, MD, USA). The targeted regions in the midbrains were outlined by the polygon selector. We reduced the noise using the 'Image>Adjust> Threshold' command accordingly (Sidi et al., 2008). After that, the 'Analyze>Analyze Particles' commands were executed, and the Size (Micro ^2) was set as 1-infinity. The data were obtained by running 'Display Results, Clear Results' and 'Summarize' programs at the same time. Finally, the ratio of the marked AO^{+} area in the whole outlined midbrain region was calculated using the 'Area Fraction' program. Midbrain area was measured as described previously (Chowdhury et al., 2018). In brief, zebrafish embryos at the desired stages were anaesthetized by tricaine. The brains were imaged by a digital camera (Axiocam 506 color, Carl Zeiss) in a Discovery.V20 microscope (Carl Zeiss). The images were analyzed by ImageJ software. The 'Straight' tool was used to describe the scale. The 'Analyze>Set Scale' option was used to calculate the actual size of the whole image. Then, the 'Polygon Selection' tool was applied to determine the targeted region and the volume was given out by running the 'Analyze>Measure' command. To evaluate the zebrafish survival ratio, embryos in each group were assigned to different tanks and cultured at 28.5°C. The numbers of surviving and dead larval fish were counted daily from 3 to 10 dpf. The fresh water for larval culture was supplied regularly to avoid environmental turbidity and hypoxia. Finally, GraphPad Prism 6.01 was used to draw the survival curve, and survival distribution was estimated by the Kaplan–Meier method.

Gray value and fluorescence intensity measurement

The bands of western blotting and DNA gel electrophoresis were quantified by ImageJ software. Briefly, the 'Process>Subtract Background>80' command was executed to reduce the background. The rectangle tool was

used to outline the measured bands. The gray values of the bands were given out by the 'Analyze>Gels>Select First Lane> Select Last Lane>Plot Plane' commands. To quantify the FISH fluorescence intensity, the 'Image>Adjust>Auto Threshold' instructions were followed. Then, the 'Analyze>Set Measurements>Area>Mean Gray Value>Limit To Threshold>Mode Yen' were selected. The intensity results were calculated by the 'Analyze>Measure' commands.

Quantification and statistical analysis

scRNA-seq statistical analyses were performed in RStudio (version 4.0.3/4.0.4). The quantified data were double confirmed and analyzed by GraphPad Prism 6.01. The detailed statistical methods are included in the corresponding figure legends. Briefly, unpaired two-tailed Student's *t*-test was performed to compare two data groups without any treatment; two-way ANOVA was employed to weight the two data groups in different conditions; and one-way ANOVA was performed to analyze the data of multiple groups. Survival ratio was calculated by Kaplan–Meier calculations. Error bars indicate s.e.m. All statistical tests, *P*-values and *n* numbers are stated in figure legends

Acknowledgements

We thank H. Li and M. Ma for biochemistry analysis and discussions, Z. Cao for the *tars1*^{cq16} mutant, and H. Huang and H. Ruan for technical assistance.

Competing interests

The authors declare no competing or financial interests.

Author contributions

Conceptualization: B.J., L.Z., C.Z., L. Luo, L. Li; Methodology: B.J., L.X., D.Z., L.Z., Z.F., J.H., J.Q., C.Z., L. Luo, L. Li; Software: J.H.; Validation: L.X., D.Z.; Formal analysis: J.Q.; Investigation: B.J., L.X., D.Z., L.Z., L. Li; Resources: Z.F., J.Q., L. Luo, L. Li; Data curation: B.J., D.Z., L.Z., C.Z.; Writing - original draft: B.J.; Writing - review & editing: L. Li; Supervision: L. Luo, L. Li; Project administration: B.J., L. Luo, L. Li; Funding acquisition: L. Li.

Funding

This work was supported by grants from the National Key Research and Development Program of China (2019YFA802703) and the National Natural Science Foundation of China (31822033, 31771623).

Data availability

All raw data are deposited to Gene Expression Omnibus (GEO) under the accession number GSE196846.

Peer review history

The peer review history is available online at https://journals.biologists.com/dev/lookup/doi/10.1242/dev.200342.reviewer-comments.pdf

References

Alunni, A., Krecsmarik, M., Bosco, A., Galant, S., Pan, L., Moens, C. B. and Bally-Cuif, L. (2013). Notch3 signaling gates cell cycle entry and limits neural stem cell amplification in the adult pallium. *Development* **140**, 3335-3347. doi:10.1242/dev.095018

Ansari, S. S., Sharma, A. K., Soni, H., Ali, D. M., Tews, B., König, R., Eibl, H. and Berger, M. R. (2018). Induction of ER and mitochondrial stress by the alkylphosphocholine erufosine in oral squamous cell carcinoma cells. *Cell Death Dis.* **9**, 296. doi:10.1038/s41419-018-0342-2

Atkins, C., Liu, Q., Minthorn, E., Zhang, S.-Y., Figueroa, D. J., Moss, K., Stanley, T. B., Sanders, B., Goetz, A., Gaul, N. et al. (2013). Characterization of a novel PERK kinase inhibitor with antitumor and antiangiogenic activity. *Cancer Res.* **73**, 1993-2002. doi:10.1158/0008-5472.CAN-12-3109

Balaji, N., Devy, A. S., Sumathi, M. K., Vidyalakshmi, S., Kumar, G. S. and D'Silva, S. (2013). Annexin v - affinity assay - apoptosis detection system in granular cell ameloblastoma. *J. Int. Oral Health* **5**, 25-30.

Baumel-Alterzon, S., Katz, L. S., Brill, G., Garcia-Ocaña, A. and Scott, D. K. (2021). Nrf2: the master and captain of beta cell fate. *Trends Endocrinol. Metab.* **32**, 7-19. doi:10.1016/j.tem.2020.11.002

Binet, F. and Sapieha, P. (2015). ER Stress and Angiogenesis. *Cell Metab.* **22**, 560-575. doi:10.1016/j.cmet.2015.07.010

Bonay, M., Roux, A.-L., Floquet, J., Retory, Y., Herrmann, J.-L., Lofaso, F. and Deramaudt, T. B. (2015). Caspase-independent apoptosis in infected macrophages triggered by sulforaphane via Nrf2/p38 signaling pathways. *Cell Death Discovery* **1**, 15022. doi:10.1038/cddiscovery.2015.22

Butler, A., Hoffman, P., Smibert, P., Papalexi, E. and Satija, R. (2018). Integrating single-cell transcriptomic data across different conditions, technologies, and species. *Nat. Biotechnol.* **36**, 411-420. doi:10.1038/nbt.4096

Cao, Z., Wang, H., Mao, X. and Luo, L. (2016). Noncanonical function of threonyl-tRNA synthetase regulates vascular development in zebrafish. *Biochem. Biophys. Res. Commun.* **473**, 67-72. doi:10.1016/j.bbrc.2016.03.051

Chang, N., Sun, C., Gao, L., Zhu, D., Xu, X., Zhu, X., Xiong, J.-W. and Xi, J. J. (2013). Genome editing with RNA-guided Cas9 nuclease in zebrafish embryos. *Cell Res.* **23**, 465-472. doi:10.1038/cr.2013.45

Chang, C.-W., Chen, Y.-S., Tsay, Y.-G., Han, C.-L., Chen, Y.-J., Yang, C.-C., Hung, K.-F., Lin, C.-H., Huang, T.-Y., Kao, S.-Y. et al. (2018). ROS-independent ER stress-mediated NRF2 activation promotes warburg effect to maintain stemness-associated properties of cancer-initiating cells. *Cell Death Dis.* **9**, 194. doi:10.1038/s41419-017-0250-x

Cheruiyot, A., Li, S., Srivatsan, S. N., Ahmed, T., Chen, Y. H., Lemacon, D. S., Li, Y., Yang, Z., Wadugu, B. A., Warner, W. A. et al. (2021). Nonsense-mediated RNA decay is a unique vulnerability of cancer cells harboring SF3B1 or U2AF1 mutations. *Cancer Res.* **81**, 4499-4513. doi:10.1158/0008-5472.CAN-20-4016

Chowdhury, T. A., Koceja, C., Eisa-Beygi, S., Kleinstiver, B. P., Kumar, S. N., Lin, C.-W., Li, K., Prabhudesai, S., Joung, J. K. and Ramchandran, R. (2018). Temporal and spatial post-transcriptional regulation of Zebrafish tie1 mRNA by long noncoding RNA during brain vascular assembly. *Arterioscler. Thromb. Vasc. Biol.* **38**, 1562-1575. doi:10.1161/ATVBAHA.118.310848

Durruthy-Durruthy, R. and Heller, S. (2015). Applications for single cell trajectory analysis in inner ear development and regeneration. *Cell Tissue Res.* **361**, 49-57. doi:10.1007/s00441-014-2079-2

Fernández-Millán, E., Martín, M. A., Goya, L., Lizárraga-Mollinedo, E., Escrivá, F., Ramos, S. and Álvarez, C. (2016). Glucagon-like peptide-1 improves beta-cell antioxidant capacity via extracellular regulated kinases pathway and Nrf2 translocation. *Free Radic. Biol. Med.* **95**, 16-26. doi:10.1016/j.freeradbiomed.2016.03.002

Fu, S., Yalcin, A., Lee, G. Y., Li, P., Fan, J., Arruda, A. P., Pers, B. M., Yilmaz, M., Eguchi, K. and Hotamisligil, G. S. (2015). Phenotypic assays identify azoramide as a small-molecule modulator of the unfolded protein response with antidiabetic activity. *Sci. Transl. Med.* **7**, 292ra298.

Gallagher, C. M., Garri, C., Cain, E. L., Ang, K. K.-H., Wilson, C. G., Chen, S., Hearn, B. R., Jaishankar, P., Aranda-Diaz, A., Arkin, M. R. et al. (2016). Ceapins are a new class of unfolded protein response inhibitors, selectively targeting the ATF6α branch. *eLife* **5**, e11878. doi:10.7554/eLife.11878

Grandjean, J. M. D., Madhavan, A., Cech, L., Seguinot, B. O., Paxman, R. J., Smith, E., Scampavia, L., Powers, E. T., Cooley, C. B., Plate, L. et al. (2020). Pharmacologic IRE1/XBP1s activation confers targeted ER proteostasis reprogramming. *Nat. Chem. Biol.* **16**, 1052-1061. doi:10.1038/s41589-020-0584-z

Guha, P., Kaptan, E., Gade, P., Kalvakolanu, D. V. and Ahmed, H. (2017). Tunicamycin induced endoplasmic reticulum stress promotes apoptosis of prostate cancer cells by activating mTORC1. *Oncotarget* **8**, 68191-68207. doi:10.18632/oncotarget.19277

Guo, F.-J., Xiong, Z., Lu, X., Ye, M., Han, X. and Jiang, R. (2014). ATF6 upregulates XBP1S and inhibits ER stress-mediated apoptosis in osteoarthritis cartilage. *Cell. Signal.* **26**, 332-342. doi:10.1016/j.cellsig.2013.11.018

He, J., Mo, D., Chen, J. and Luo, L. (2020). Combined whole-mount fluorescence in situ hybridization and antibody staining in zebrafish embryos and larvae. *Nat. Protoc.* **15**, 3361-3379. doi:10.1038/s41596-020-0376-7

Hesselson, D., Anderson, R. M., Beinat, M. and Stainier, D. Y. R. (2009). Distinct populations of quiescent and proliferative pancreatic beta-cells identified by HOTcre mediated labeling. *Proc. Natl. Acad. Sci. USA* **106**, 14896-14901. doi:10.1073/pnas.0906348106

Hu, H., Tian, M., Ding, C. and Yu, S. (2018). The C/EBP Homologous Protein (CHOP) transcription factor functions in endoplasmic reticulum stress-induced apoptosis and microbial infection. *Front. Immunol.* **9**, 3083. doi:10.3389/fimmu.2018.03083

Huang, Y., Lu, Y., He, Y., Feng, Z., Zhan, Y., Huang, X., Liu, Q., Zhang, J., Li, H., Huang, H. et al. (2019). Ikzf1 regulates embryonic T lymphopoiesis via Ccr9 and Irf4 in zebrafish. *J. Biol. Chem.* **294**, 16152-16163. doi:10.1074/jbc.RA119.009883

Humeau, J., Leduc, M., Cerrato, G., Loos, F. and Kroemer, G. (2020). Phosphorylation of eukaryotic initiation factor-2α (eIF2α) in autophagy. *Cell Death Dis.* **11**, 433. doi:10.1038/s41419-020-2642-6

Jia, X.-E., Ma, K., Xu, T., Gao, L., Wu, S., Fu, C., Zhang, W., Wang, Z., Liu, K., Dong, M. et al. (2015). Mutation of kri1l causes definitive hematopoiesis failure via PERK-dependent excessive autophagy induction. *Cell Res.* **25**, 946-962. doi:10.1038/cr.2015.81

Kang, K. A., Piao, M. J., Hyun, Y. J., Zhen, A. X., Cho, S. J., Ahn, M. J., Yi, J. M. and Hyun, J. W. (2019). Luteolin promotes apoptotic cell death via upregulation of Nrf2 expression by DNA demethylase and the interaction of Nrf2 with p53 in human colon cancer cells. *Exp. Mol. Med.* **51**, 1-14. doi:10.1038/s12276-019-0238-y

Kawai, Y., Garduño, L., Theodore, M., Yang, J. and Arinze, I. J. (2011). Acetylation-deacetylation of the transcription factor Nrf2 (nuclear factor erythroid 2-related factor 2) regulates its transcriptional activity and nucleocytoplasmic localization. *J. Biol. Chem.* **286**, 7629-7640. doi:10.1074/jbc.M110.208173

Klinge, S., Voigts-Hoffmann, F., Leibundgut, M., Arpagaus, S. and Ban, N. (2011). Crystal structure of the eukaryotic 60S ribosomal subunit in complex with initiation factor 6. *Science* **334**, 941-948. doi:10.1126/science.1211204

Kroll, F., Powell, G. T., Ghosh, M., Gestri, G., Antinucci, P., Hearn, T. J., Tunbak, H., Lim, S., Dennis, H. W., Fernandez, J. M. et al. (2021). A simple and effective F0 knockout method for rapid screening of behaviour and other complex phenotypes. *eLife* **10**, e59683. doi:10.7554/eLife.59683

Lee, J. W., Beebe, K., Nangle, L. A., Jang, J., Longo-Guess, C. M., Cook, S. A., Davisson, M. T., Sundberg, J. P., Schimmel, P. and Ackerman, S. L. (2006). Editing-defective tRNA synthetase causes protein misfolding and neurodegeneration. *Nature* **443**, 50-55. doi:10.1038/nature05096

Lei, L., Yan, S.-Y., Yang, R., Chen, J.-Y., Li, Y., Bu, Y., Chang, N., Zhou, Q., Zhu, X., Li, C.-Y. et al. (2017). Spliceosomal protein eftud2 mutation leads to p53-dependent apoptosis in zebrafish neural progenitors. *Nucleic Acids Res.* **45**, 3422-3436. doi:10.1093/nar/gkw1043

Li, L., Yan, B., Shi, Y.-Q., Zhang, W.-Q. and Wen, Z.-L. (2012). Live imaging reveals differing roles of macrophages and neutrophils during zebrafish tail fin regeneration. *J. Biol. Chem.* **287**, 25353-25360. doi:10.1074/jbc.M112.349126

Li, J., Shang, Y., Wang, L., Zhao, B., Sun, C., Li, J., Liu, S., Li, C., Tang, M., Meng, F. L. et al. (2020). Genome integrity and neurogenesis of postnatal hippocampal neural stem/progenitor cells require a unique regulator Filia. *Sci. Adv.* **6**, eaba0682. doi:10.1126/sciadv.aba0682

Liu, Y., Satz, J. S., Vo, M.-N., Nangle, L. A., Schimmel, P. and Ackerman, S. L. (2014). Deficiencies in tRNA synthetase editing activity cause cardioproteinopathy. *Proc. Natl. Acad. Sci. USA* **111**, 17570-17575. doi:10.1073/pnas.1420196111

Ma, Q. (2013). Role of nrf2 in oxidative stress and toxicity. *Annu. Rev. Pharmacol. Toxicol.* **53**, 401-426. doi:10.1146/annurev-pharmtox-011112-140320

Magesh, S., Chen, Y. and Hu, L. (2012). Small molecule modulators of Keap1-Nrf2-ARE pathway as potential preventive and therapeutic agents. *Med. Res. Rev.* **32**, 687-726. doi:10.1002/med.21257

Marquez-Legorreta, E., Piber, M. and Scott, E. K. (2020). Visual escape in larval zebrafish: stimuli, circuits, and behavior. Behavioral and Neural Genetics of Zebrafish.

McLaughlin, H. M., Sakaguchi, R., Giblin, W., Program, N. C. S., Wilson, T. E., Biesecker, L., Lupski, J. R., Talbot, K., Vance, J. M., Züchner, S. et al. (2012). A recurrent loss-of-function alanyl-tRNA synthetase (AARS) mutation in patients with Charcot-Marie-Tooth disease type 2N (CMT2N). *Hum. Mutat.* **33**, 244-253. doi:10.1002/humu.21635

Menegon, S., Columbano, A. and Giordano, S. (2016). The dual roles of NRF2 in cancer. *Trends Mol. Med.* **22**, 578-593. doi:10.1016/j.molmed.2016.05.002

Metcalf, M. G., Higuchi-Sanabria, R., Garcia, G., Tsui, C. K. and Dillin, A. (2020). Beyond the cell factory: homeostatic regulation of and by the UPR(ER). *Sci. Adv.* **6**, eabb9614. doi:10.1126/sciadv.abb9614

Mohamed, E., Sierra, R. A., Trillo-Tinoco, J., Cao, Y., Innamarato, P., Payne, K. K., de Mingo Pulido, A., Mandula, J., Zhang, S., Thevenot, P. et al. (2020). The Unfolded Protein Response Mediator PERK Governs Myeloid Cell-Driven Immunosuppression in Tumors through Inhibition of STING Signaling. *Immunity* **52**, 668-682.e67. doi:10.1016/j.immuni.2020.03.004

Motley, W. W., Griffin, L. B., Mademan, I., Baets, J., De Vriendt, E., De Jonghe, P., Antonellis, A., Jordanova, A. and Scherer, S. S. (2015). A novel AARS mutation in a family with dominant myeloneuropathy. *Neurology* **84**, 2040-2047. doi:10.1212/WNL.0000000000001583

Mukaigasa, K., Tsujita, T., Nguyen, V. T., Li, L., Yagi, H., Fuse, Y., Nakajima-Takagi, Y., Kato, K., Yamamoto, M. and Kobayashi, M. (2018). Nrf2 activation attenuates genetic endoplasmic reticulum stress induced by a mutation in the phosphomannomutase 2 gene in zebrafish. *Proc. Natl. Acad. Sci. USA* **115**, 2758-2763. doi:10.1073/pnas.1714056115

Ohtsubo, T., Kamada, S., Mikami, T., Murakami, H. and Tsujimoto, Y. (1999). Identification of NRF2, a member of the NF-E2 family of transcription factors, as a substrate for caspase-3(-like) proteases. *Cell Death Differ.* **6**, 865-872. doi:10.1038/sj.cdd.4400566

Palmér, T., Ek, F., Enqvist, O., Olsson, R., Astrom, K. and Petersson, P. (2017). Action sequencing in the spontaneous swimming behavior of zebrafish larvae - implications for drug development. *Sci. Rep.* **7**, 3191. doi:10.1038/s41598-017-03144-7

Pobre, K. F. R., Poet, G. J. and Hendershot, L. M. (2019). The endoplasmic reticulum (ER) chaperone BiP is a master regulator of ER functions: Getting by with a little help from ERdj friends. *J. Biol. Chem.* **294**, 2098-2108. doi:10.1074/jbc.REV118.002804

Schmidt, R., Strähle, U. and Scholpp, S. (2013). Neurogenesis in zebrafish - from embryo to adult. *Neural Dev.* **8**, 3. doi:10.1186/1749-8104-8-3

Sehgal, P., Szalai, P., Olesen, C., Praetorius, H. A., Nissen, P., Christensen, S. B., Engedal, N. and Møller, J. V. (2017). Inhibition of the sarco/endoplasmic reticulum (ER) Ca2+-ATPase by thapsigargin analogs induces cell death via ER Ca2+ depletion and the unfolded protein response. *J. Biol. Chem.* **292**, 19656-19673. doi:10.1074/jbc.M117.796920

She, J., Yuan, Z., Wu, Y., Chen, J. and Kroll, J. (2018). Targeting erythropoietin protects against proteinuria in type 2 diabetic patients and in zebrafish. *Mol. Metab.* **8**, 189-202. doi:10.1016/j.molmet.2017.11.006

Sidi, S., Sanda, T., Kennedy, R. D., Hagen, A. T., Jette, C. A., Hoffmans, R., Pascual, J., Imamura, S., Kishi, S., Amatruda, J. F. et al. (2008). Chk1 suppresses a caspase-2 apoptotic response to DNA damage that bypasses p53, Bcl-2, and caspase-3. *Cell* **133**, 864-877. doi:10.1016/j.cell.2008.03.037

Simons, C., Griffin, L. B., Helman, G., Golas, G., Pizzino, A., Bloom, M., Murphy, J. L. P., Crawford, J., Evans, S. H., Topper, S. et al. (2015). Loss-of-function alanyl-tRNA synthetase mutations cause an autosomal-recessive early-onset epileptic encephalopathy with persistent myelination defect. *Am. J. Hum. Genet.* **96**, 675-681. doi:10.1016/j.ajhg.2015.02.012

Stuart, T., Butler, A., Hoffman, P., Hafemeister, C., Papalexi, E., Mauck, W. M., III, Hao, Y., Stoeckius, M., Smibert, P. and Satija, R. (2019). Comprehensive Integration of Single-Cell Data. *Cell* **177**, 1888-1902.e21. doi:10.1016/j.cell.2019.05.031

Sztal, T. E., Ruparelia, A. A., Williams, C. and Bryson-Richardson, R. J. (2016). Using touch-evoked response and locomotion assays to assess muscle performance and function in zebrafish. *J. Vis. Exp.* 54431. doi:10.3791/54431

Tambalo, M., Mitter, R. and Wilkinson, D. G. (2020). A single cell transcriptome atlas of the developing zebrafish hindbrain. *Development* **147**, dev184143. doi:10.1242/dev.184143

Tamura, K., Peterson, D., Peterson, N., Stecher, G., Nei, M. and Kumar, S. (2011). MEGA5: molecular evolutionary genetics analysis using maximum likelihood, evolutionary distance, and maximum parsimony methods. *Mol. Biol. Evol.* **28**, 2731-2739. doi:10.1093/molbev/msr121

Thomas-Jinu, S., Gordon, P. M., Fielding, T., Taylor, R., Smith, B. N., Snowden, V., Blanc, E., Vance, C., Topp, S., Wong, C.-H. et al. (2017). Non-nuclear pool of splicing factor SFPQ regulates axonal transcripts required for normal motor development. *Neuron* **94**, 931. doi:10.1016/j.neuron.2017.04.036

Thompson, R., Shah, R. B., Liu, P. H., Gupta, Y. K., Ando, K., Aggarwal, A. K. and Sidi, S. (2015). An Inhibitor of PIDDosome Formation. *Mol. Cell* **58**, 767-779. doi:10.1016/j.molcel.2015.03.034

Tilton, F. and Tanguay, R. L. (2008). Exposure to sodium metam during zebrafish somitogenesis results in early transcriptional indicators of the ensuing neuronal and muscular dysfunction. *Toxicol. Sci.* **106**, 103-112. doi:10.1093/toxsci/kfn145

Timme-Laragy, A. R., Karchner, S. I., Franks, D. G., Jenny, M. J., Harbeitner, R. C., Goldstone, J. V., McArthur, A. G. and Hahn, M. E. (2012). Nrf2b, novel zebrafish paralog of oxidant-responsive transcription factor NF-E2-related factor 2 (NRF2). *J. Biol. Chem.* **287**, 4609-4627. doi:10.1074/jbc.M111.260125

Trevarrow, B. (2011). Techniques for optimizing the creation of mutations in zebrafish using N-ethyl-N-nitrosourea. *Lab. Anim.* **40**, 353-361. doi:10.1038/laban1111-353

Vo, M.-N., Terrey, M., Lee, J. W., Roy, B., Moresco, J. J., Sun, L., Fu, H., Liu, Q., Weber, T. G., Yates, J. R.III et al. (2018). ANKRD16 prevents neuron loss caused by an editing-defective tRNA synthetase. *Nature* **557**, 510-515. doi:10.1038/s41586-018-0137-8

Walter, P. and Ron, D. (2011). The unfolded protein response: from stress pathway to homeostatic regulation. *Science* **334**, 1081-1086. doi:10.1126/science.1209038

Wang, M. and Kaufman, R. J. (2016). Protein misfolding in the endoplasmic reticulum as a conduit to human disease. *Nature* **529**, 326-335. doi:10.1038/nature17041

Wang, J., Lee, J., Liem, D. and Ping, P. (2017). HSPA5 Gene encoding Hsp70 chaperone BiP in the endoplasmic reticulum. *Gene* **618**, 14-23. doi:10.1016/j.gene.2017.03.005

Wu, Y.-C. and Wang, I.-J. (2020). Heat-shock-induced tyrosinase gene ablation with CRISPR in zebrafish. *Mol. Genet. Genomics* **295**, 911-922. doi:10.1007/s00438-020-01681-x

Wu, S., Xue, R., Hassan, S., Thi My Linh, N., Wang, T., Pan, H., Xu, J., Liu, Q., Zhang, W. and Wen, Z. (2018). Il34-Csf1r pathway regulates the migration and colonization of microglial precursors. *Dev. Cell* **46**, 552-563.e54. doi:10.1016/j.devcel.2018.08.005

Xue, Y., Liu, D., Cui, G., Ding, Y., Ai, D., Gao, S., Zhang, Y., Suo, S., Wang, X., Lv, P. et al. (2019). A 3D atlas of hematopoietic stem and progenitor cell expansion by multi-dimensional RNA-Seq analysis. *Cell Rep.* **27**, 1567-1578.e65. doi:10.1016/j.celrep.2019.04.030

You, K., Wang, L., Chou, C.-H., Liu, K., Nakata, T., Jaiswal, A., Yao, J., Lefkovith, A., Omar, A., Perrigoue, J. G. et al. (2021). QRICH1 dictates the outcome of ER stress through transcriptional control of proteostasis. *Science* **371**, eabb6896. doi:10.1126/science.abb6896

Yu, G., Wang, L.-G., Han, Y. and He, Q.-Y. (2012). clusterProfiler: an R package for comparing biological themes among gene clusters. *OMICS* **16**, 284-287. doi:10.1089/omi.2011.0118

Yu, Z., Sheng, H., Liu, S., Zhao, S., Glembotski, C. C., Warner, D. S., Paschen, W. and Yang, W. (2017). Activation of the ATF6

branch of the unfolded protein response in neurons improves stroke outcome. *J. Cereb. Blood Flow Metab.* **37**, 1069-1079. doi:10.1177/0271678X16650218

Zhao, F., Shi, Y., Huang, Y., Zhan, Y., Zhou, L., Li, Y., Wan, Y., Li, H., Huang, H., Ruan, H. et al. (2018). Irf8 regulates the progression of myeloproliferative neoplasm-like syndrome via Mertk signaling in zebrafish. *Leukemia* **32**, 149-158. doi:10.1038/leu.2017.189

Zou, J. and Wei, X. (2010). Transplantation of GFP-expressing blastomeres for live imaging of retinal and brain development in chimeric zebrafish embryos. *J. Vis. Exp.* 1924. doi:10.3791/1924